SPECIAL
DYNAMO/CINDY/AMIE/LASP
COLLECTION

Regional Simulation of the October and November MJO Events Observed during the CINDY/DYNAMO Field Campaign at Gray Zone Resolution

SHUGUANG WANG

Department of Applied Physics and Applied Mathematics, Columbia University, New York, New York

ADAM H. SOBEL

Department of Applied Physics and Applied Mathematics, Columbia University, New York, and Lamont-Doherty Earth Observatory, Columbia University, Palisades, and Department of Earth and Environmental Sciences, Columbia University, New York, New York

FUQING ZHANG, Y. QIANG SUN, AND YING YUE

Department of Meteorology, The Pennsylvania State University, University Park, Pennsylvania

LEI ZHOU

State Key Laboratory of Satellite Ocean Environment Dynamics, Second Institute of Oceanography, Hangzhou, China

ABSTRACT

This study investigates the October and November MJO events observed during the Cooperative Indian Ocean Experiment on Intraseasonal Variability in the Year 2011 (CINDY)/Dynamics of the MJO (DYNAMO) field campaign through cloud-permitting numerical simulations. The simulations are compared to multiple observational datasets. The control simulation at 9-km horizontal grid spacing captures the slow eastward progression of both the October and November MJO events in surface precipitation, outgoing longwave radiation, zonal wind, humidity, and large-scale vertical motion. The vertical motion shows weak ascent in the leading edge of the MJO envelope, followed by deep ascent during the peak precipitation stage and trailed by a broad second baroclinic mode structure with ascent in the upper troposphere and descent in the lower troposphere. Both the simulation and the observations also show slow northward propagation components and tropical cyclone–like vortices after the passage of the MJO active phase. Comparison with synthesized observations from the northern sounding array shows that the model simulates the passage of the two MJO events over the sounding array region well. Sensitivity experiments to SST indicate that daily SST plays an important role for the November MJO event, but much less so for the October event.

Analysis of the moist static energy (MSE) budget shows that both advection and diabatic processes (i.e., surface fluxes and radiation) contribute to the development of the positive MSE anomaly in the active phase, but their contributions differ by how much they lead the precipitation peak. In comparison to the observational datasets used here, the model simulation may have a stronger surface flux feedback and a weaker radiative feedback. The normalized gross moist stability in the simulations shows an increase from near-zero values to ~0.8 during the active phase, similar to what is found in the observational datasets.

1. Introduction

The Madden–Julian oscillation (MJO; Madden and Julian 1971, 1972) is an intraseasonal weather phenomenon in the tropics. Because of its influence on global weather and climate (Zhang 2005), understanding, simulation, and prediction of the MJO have great scientific and societal value.

Modeling and prediction of MJO initiation in the Indian Ocean remains a long standing challenge. The field campaign Cooperative Indian Ocean Experiment on Intraseasonal Variability in the Year 2011 (CINDY)/Dynamics

Corresponding author address: Shuguang Wang, Department of Applied Physics and Applied Mathematics, Columbia University, New York, NY 10025.
E-mail: sw2526@columbia.edu

of the MJO (DYNAMO)/ARM MJO Investigation Experiment (AMIE) (hereinafter DYNAMO for brevity) was designed specifically to address this issue. The DYNAMO observational network captured four MJO events from October 2011 to March 2012 (Zhang et al. 2013; Yoneyama et al. 2013; Gottschalck et al. 2013).

New findings emerging from DYNAMO have been reported in a number of studies that document various aspects of these MJO events in the Indian Ocean, including the large-scale structure of dynamical variables (temperature, zonal winds, humidity, and vertical motion) derived from the sounding network (Johnson and Ciesielski 2013; Ciesielski et al. 2014), the cloud population observed from the ground-based precipitation radars (e.g., Zuluaga and Houze 2013; Powell and Houze 2013), the air and sea processes regulating the atmosphere–ocean interaction (Moum et al. 2013), and the budget of moist static energy in the northern sounding array (Sobel et al. 2014, hereafter S14). Attempts have been made in these observational studies to infer the roles of different components of the coupled atmosphere–ocean system for the MJO initiation and propagation. Yet, the precise mechanisms responsible for the initiation and propagation of these MJO events remain elusive.

A variety of theoretical models has been proposed in the past, emphasizing various different processes. An incomplete and selective list includes frictional boundary layer moisture convergence (Wang 1988; Wang and Rui 1990), surface enthalpy fluxes (Emanuel 1987; Neelin et al. 1987), radiative feedback (Hu and Randall 1994; Raymond 2001; Bony and Emanuel 2005), a combination of both surface turbulent enthalpy fluxes and radiative feedback as sources of moist static energy (Sobel et al. 2008, 2010), and moisture modes coupling temporal and spatial variation of moisture with dry dynamics (e.g., Sobel et al. 2001; Sobel and Maloney 2012, 2013; Fuchs and Raymond 2002; Raymond and Fuchs 2007; Majda and Stechmann 2009). Although none of these has been accepted as fully satisfactory by the research community as a whole, the recent development of these MJO theories has converged attention on the prominent role of free-tropospheric moisture. The idea that free-tropospheric moisture variations are important to the MJO has been reinforced by many studies demonstrating that numerical models in which deep convection is more sensitive to free-tropospheric moisture produce better MJO simulations (e.g., Thayer-Calder and Randall 2009).

The representation of the MJO in the comprehensive climate models used for climate assessment has improved relatively slowly (e.g., Lin et al. 2006; Hung et al. 2013). This may be partly because parameterization changes that would improve the MJO simulation tend to degrade some aspects of the mean climate and are seen as undesirable

for the purposes of assessments (Kim et al. 2011); nonetheless, it indicates a structural problem in the models. On the other hand, a number of recent process oriented studies have been performed using high-resolution regional models (Ray et al. 2009; Holloway et al. 2013; Khouider and Han 2013; Hagos and Leung 2011; Hagos et al. 2011). The focused view offered by such models is attractive because convection and its coupling with large-scale dynamics are better expressed in those models than in lower-resolution models in which convection is highly parameterized. An additional benefit of using a regional model is that error outside the region of interest may be minimized by prescribing boundary conditions directly from the analysis/reanalysis dataset, further improving the MJO simulation skill (e.g., Ray et al. 2009; Ray and Zhang 2010). While this is not prediction skill—since it requires knowledge of the boundary conditions—it allows detailed for analysis of a simulated MJO that is internally consistent (to the extent that the model budgets close); contains information on finer scales than a global climate model would; and, to the extent the simulations are successful, can bear close resemblance to the observed MJO.

In this study, a cloud-permitting regional modeling system, combined with several observational datasets, is used to 1) simulate the MJO events that occurred during DYNAMO and further document their multiscale variability, 2) validate the simulation of the mean state and intraseasonal variability using the observational datasets, and 3) construct the budgets of moisture and moist static energy of the simulated MJO events. Our resolution lies in the "gray zone," in which convective updrafts are not well resolved but mesoscale convective systems are, and we use no convective parameterization. What phenomena can be simulated at this resolution, with what strengths and weaknesses, is an area of active research (e.g., Miura et al. 2007; Yu and Lee 2010; Jung et al. 2012; Miyakawa et al. 2014). Observational validation in this study will serve as a stepping stone to future numerical experiments exploring the dynamics of these MJO events with the model configuration we use here.

The rest of this paper is structured as follows: Section 2 has the details of the numerical model configuration, experimental design, and observational datasets. Section 3 contains the description of the observed and simulated MJO events. Section 4 describes the moisture and moist static energy budgets. Results are summarized in section 5.

2. Numerical experiments and observation dataset

a. Numerical model and experiment design

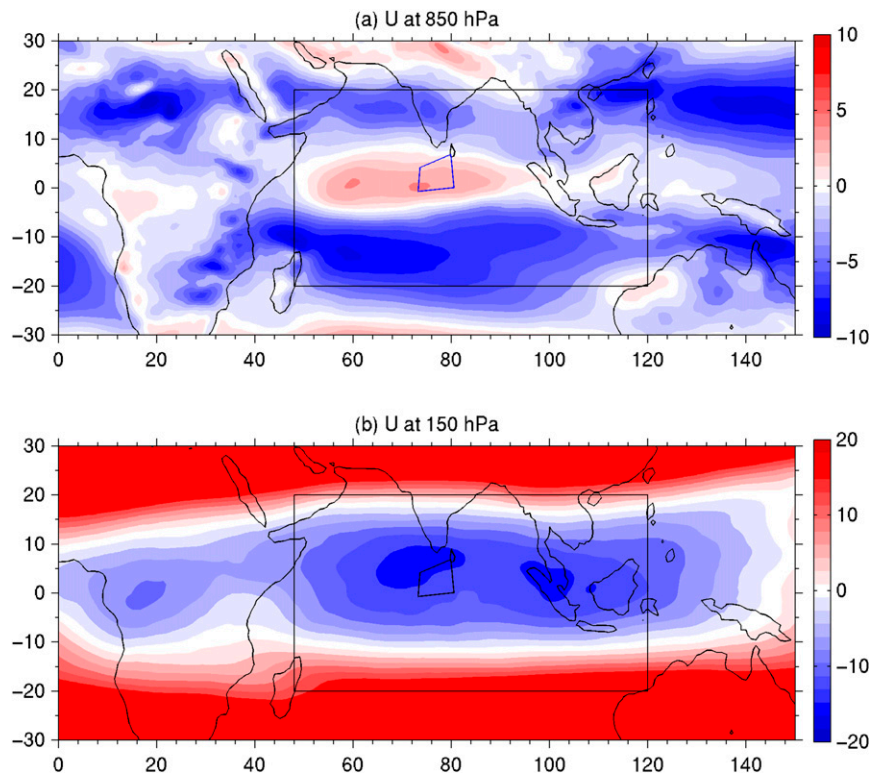The Weather Research and Forecasting Model version 3.4.1 (WRF3.4.1; Skamarock et al. 2008) is used in this

FIG. 1. (a) 850- and (b) 150-hPa zonal winds (m s^{-1}) averaged from October to December. The WRF domain is indicated by the black rectangle. The blue polygon indicates the area of NSA.

study. ERA-Interim (Dee et al. 2011) is adopted to construct the initial, bottom, and lateral boundary conditions for the regional simulation. The lateral boundary consists of a narrow transition zone of 5 grid points, where the tendencies at the outmost grids are prescribed from ERA-Interim every 6 h, and gradually merged with the tendencies generated by the model.

At the oceanic portion of the lower boundary, SST is updated every 6 h using the ERA-Interim SST. Additional sensitivity experiments are also conducted in which time-averaged SST is used (section 3d). Surface temperature over land is allowed to vary using the unified Noah land surface physics scheme (Chen and Dudhia 2001). The surface skin temperature as a separate variable is diagnosed using the surface skin temperature scheme (Zeng and Beljaars 2005). This creates diurnally varying surface temperature over both ocean and land. The GCM version of the Rapid Radiative Transfer Model (RRTMG) longwave radiation scheme (Iacono et al. 2008) and the updated Goddard shortwave scheme (Chou and Suarez 1994; T. Matsui et al. 2007, meeting presentation; Shi et al. 2010) are used to parameterize radiative processes. Subgrid-scale vertical turbulent eddy mixing is parameterized using the Yonsei University (YSU) PBL scheme (Hong et al. 2006). Surface fluxes are treated using the Monin–Obukov scheme. The WRF Double-Moment (WDM) microphysics

scheme (Lim and Hong 2010) from WRF3.5.1 is adopted with additional modification on the limit of the shape parameters and terminal speed of snow, based on preliminary tests and our experience in cloud-resolving simulations. No convective parameterization scheme is used.

The horizontal and vertical advection schemes are fifth-order and third-order accurate, respectively. Moisture and condensate are advected using a positive definite scheme. The implicit damping scheme is used to suppress unphysical reflection of vertically propagating gravity waves in the top 5 km (Klemp et al. 2008). The horizontal turbulent eddy mixing is parameterized using the Smagorinsky first-order closure, and evaluated in the physical space.

The computational domain covers the equatorial Indian Ocean, from 20°S to 20°N and from 48° to 120°E, as shown in Fig. 1a. The vertical is discretized in to 45 vertical levels, with 9 levels in the lowest 1 km and a nominal top at 20 hPa. Horizontal grid spacing is chosen to be 9 km, in the so-called gray zone. This is not adequate for individual convective cells, but can partly resolve organized cloud systems and mesoscale circulations, as well as their upscale impact and coupling with large-scale dynamics.

The model simulations start from 1 October 2011. For the first 3 days, horizontal winds are relaxed to ERA-Interim using spectral nudging with a zonal wavenumber

0–4 (>2000 km; wavenumber is defined relative to the computational domain) and a meridional wavenumber 0–2 (>2000 km). No nudging is used for other variables. This nudging does not introduce additional sources/ sinks for moisture but tightly constrains the mean flow and horizontal convergence over the largest scales in the domain. This 3-day spectral nudging also allows the mesoscale to saturate in spectral space. After 4 October, the model is integrated to 15 December 2011 without any further nudging. We focus on the free run period from 4 October to the end of the simulation.

b. Observational datasets

A number of observational datasets are used to study the two MJO events and to validate our simulations. The large-scale dataset derived from the DYNAMO northern sounding array (NSA; Johnson and Ciesielski 2013; Ciesielski et al. 2014) provides time evolution of the vertical structures within the area covered by the array. Large-scale horizontal flow fields are extracted from the ERA-Interim dataset. Surface rainfall is taken from the 3-hourly 0.25° TRMM 3B42 rainfall product version 7A. The 8-km CPC morphing technique (CMORPH) rainfall dataset (Joyce et al. 2004), instead of 0.25° TRMM data, is used to construct the wavenumber–frequency diagram of rainfall, since high-frequency waves are better represented in CMORPH. Radiative fluxes are composited from the $1° \times 1°$ daily Clouds and the Earth's Radiant Energy System (CERES; Wielicki et al. 1996; Loeb et al. 2012) 1° synoptic (SYN1deg) data. Total precipitable water vapor estimated from microwave satellite observations—Special Sensor Microwave Imager (SSM/I) and Tropical Rainfall Measuring Mission Microwave Imager (TMI)—is also used for comparison with the simulations.

3. Comparison of the WRF simulation with observations

a. The spatial and temporal evolution of the MJO events

The time-mean zonal wind in the equatorial Indian Ocean was westerly in the lower troposphere and strong easterly in the upper troposphere during October and November 2011, as shown in Fig. 1. The coherent MJO events observed during the DYNAMO were strongest over the NSA and weaker south of the equator.

Figures 2a,b show a Hovmöller diagram of daily rainfall averaged between the equator and 5°N from TRMM and the WRF simulation. Both model and observations clearly show two MJO events, starting from ~60°E and propagating eastward. The October event moves with a speed of ~5 m s^{-1} while the November event moves slightly faster. The eastward propagation of

surface precipitation is greatly disrupted near the Maritime Continent (~100°E) in both the model and observations: the October event shows little propagation across the Maritime Continent in rainfall (more so in the simulation), while the November event maintains coherent propagation in both model and TRMM after passage over Sumatra (east of 100°E). MJO propagation across the Maritime Continent is poorly simulated in most climate models (e.g., Hung et al. 2013). Despite its occurrence many days after the model initialization date, the simulation correctly captures the initialization of the first event on around 16 October at 60°E and the November MJO event with a delay of ~2–3 days relative to observations.

The slow eastward progression of both MJO events in the zonal wind at 850 hPa (U850) is further shown in Fig. 3. Eastward-propagating westerlies associated with the October MJO events are apparent in both observations (Fig. 3b) and the WRF simulation (Fig. 3a). Rainfall associated with the October MJO event is not collocated with the westerly wind maximum but occurs mostly in the leading edge of the westerly regime bordering the easterlies (where there is maximum low-level zonal convergence), similar to what is seen in the observations (Figs. 3a,b). This low-level confluence also corresponds well to the MJO precipitation for the November event. The phase relation between U850 and rainfall is consistent with the conceptual model in the original work by Madden and Julian (1972) but different from what occurs in the western Pacific (Houze et al. 2000), where rainfall tends to be more nearly collocated with the westerly maximum. ERA-Interim also shows a strong westerly anomaly (~10 m s^{-1}) around 25–28 November that seems to propagate westward; a similar strong westerly anomaly is seen in the simulation in Fig. 3a without westward propagation. The largest U850 discrepancy between model and ERA-Interim is the strong westerlies in the simulation after the November event, which is not found in the observations. As this is almost 2 months after initialization, we expect that any memory of the initial conditions has been lost by this time and that the lower and lateral boundary conditions are the only significant external influences on the solution.

Figure 4 shows the vertical structure of the 3-day-averaged large-scale vertical pressure velocity (ω) along with precipitation and net column radiative cooling, all averaged between the equator and 5°N for the late October MJO events. Observational validation of large-scale vertical motion will be discussed in a later section. During 12–14 October, convection in the whole Indian Ocean is suppressed with a weak precipitation maximum (~15 mm day^{-1}) near 66°E and a region of relatively weak but broad lower-tropospheric ascent located between 65° and 85°E. During 15–17 October, when the
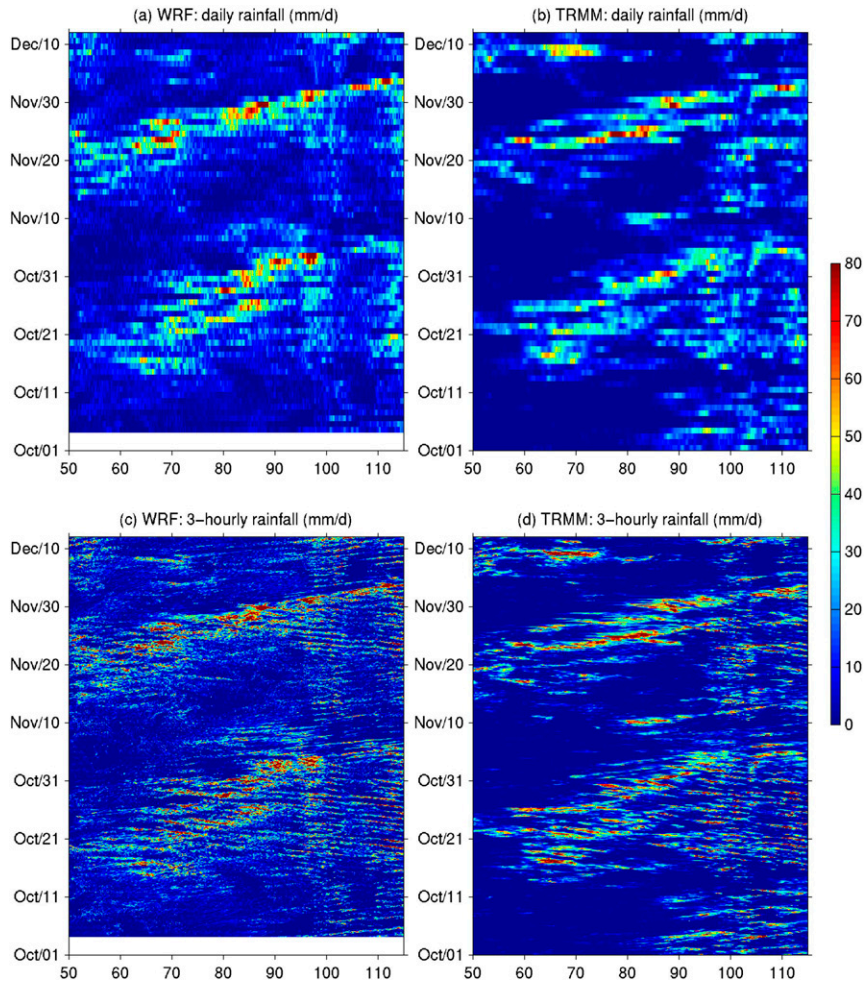
FIG. 2. Daily surface precipitation (mm day^{-1}) from (a) WRF and (b) TRMM averaged over the latitudes 0°–5°N. (c),(d) As in (a),(b), but for 3-hourly precipitation.

MJO event is already underway, vertical motion shows a westward tilt of the ascent region and a top-heavy omega profile with a distinct second baroclinic mode structure (i.e., ascent in the upper troposphere and descent in the lower troposphere) between 60° and 65°E, while the leading edge of ascent (70°–77°E) is bottom heavy. During 21–23 October, a top-heavy omega with a first baroclinic mode structure (ascent over the whole troposphere with a strong peak in the upper troposphere) is collocated with the precipitation maximum between 67° and 73°E; eastward of this region mostly bottom-heavy shallow ascent occurs, while westward of this region the second baroclinic mode structure in omega expands further. Overall, this structure—bottom-heavy ascent in the leading edge of the precipitation center, deep ascent collocated with the maximum precipitation, and ascent/descent trailing the maximum precipitation—is maintained during the entire eastward progression of the October MJO event. The ascent/descent dipole in the

vertical is coincident with a large region of strong reduced radiative cooling, presumably associated with stratiform cloud (Powell and Houze 2013). The longitudinal extent of this structure grows after the passage of the precipitation maximum. By the period of 30 October–1 November, an area of more than 20° in longitude (from 60° to 84°E) is dominated by the ascent/descent dipole. Its western edge, unlike the precipitation peak, appears to expand farther westward.

This structure of vertical motion is a reminiscent of the cross-scale self-similarity in the cloud fields shared by mesoscale convective systems, 2-day waves, synoptic convectively coupled Kelvin waves, and MJOs (Mapes et al. 2006; Kiladis et al. 2009). All have shallow clouds at the leading edge, followed by deep convective clouds and trailed by a stratiform region. The dynamical implications of this structure will be further explored in the section 4c (on the gross moist stability). The occurrence of shallow vertical motion and associated heating is
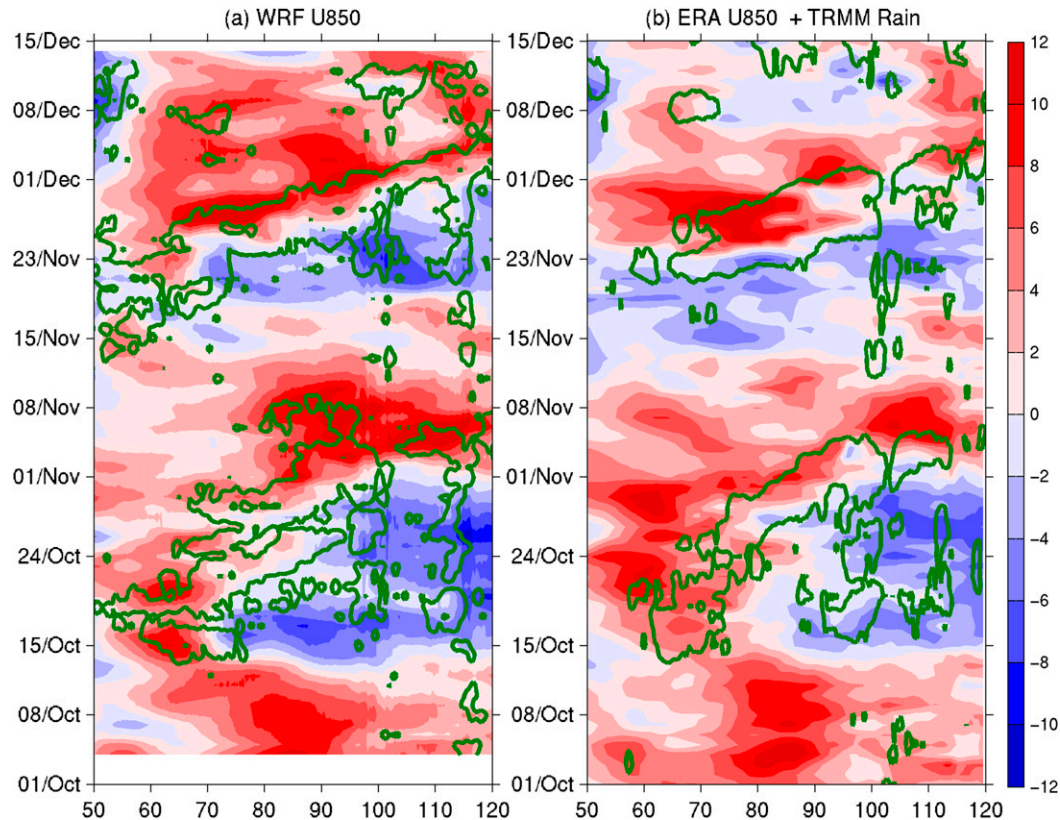
FIG. 3. Time–longitude diagram of zonal wind at 850 hPa (shading; m s^{-1}) and daily surface precipitation (contour; 15 mm day^{-1}) averaged over the latitudes 0°–5°N for (a) WRF and (b) ERA-Interim and TRMM. A 3-day moving average is applied to daily precipitation.

particularly interesting. Its role has been discussed from different perspectives: 1) a shallow, bottom-heavy vertical motion indicates that moist static energy is imported into the region, hence contributing to build up of moist static energy (e.g., Wang and Sobel 2012); 2) the circulation response to a shallow heating cannot efficiently disperse energy away horizontally because of a slow phase speed of the shallow mode (Wu 2003); and 3) more parameterized shallow heating is beneficial for improving the MJO simulations in climate models (e.g., Zhang and Song 2009). On the other hand, cloud–radiative feedback associated with the broad stratiform processes may also play a significant role in the MJO.

The November MJO event (Fig. 5) shows a similar time–longitude structure in the vertical motion but evolves at a slightly faster pace. The WRF simulation also shows that precipitation and omega associated with this MJO event do not propagate continuously but instead with a more stepwise eastward progression (e.g., from 21–23 to 27–29 November).

High-frequency variations are apparent in 3-hourly surface precipitation data. Figures 2c,d show clearly fast westward-propagating signals in both TRMM and

WRF. Some of these westward-propagating waves are prominent during the active phase of the two MJO events over the open Indian Ocean, while others are geographically linked to large islands over the Maritime Continent (e.g., Sumatra). These fast signals are in phase with diurnal variations, and closely related to the so-called 2-day waves (Zhou and Kang 2013; Tulich and Kiladis 2012), which were observed by the precipitation radar deployed at the Gan radar supersite during DYNAMO (e.g., Zuluaga and Houze 2013).

The high-frequency variability in the time–longitude diagram of 3-hourly precipitation is also apparent in spectral space. Figure 6 shows the wavenumber–frequency diagram, a regional equivalent of the global Wheeler–Kiladis diagram (Wheeler and Kiladis 1999), for the 3-hourly surface rainfall from CMORPH and WRF. A 16-day time segment with an 8-day overlap is used for the Fourier transform in the longitude range 50°–95°E and further averaged over the latitude band from 5°S to 5°N. The spectrum is normalized by applying multiple passes of a 1–2–1 filter on the wavenumber space: 40 passes in the present study. Because of the relatively short longitude and temporal windows, low-frequency
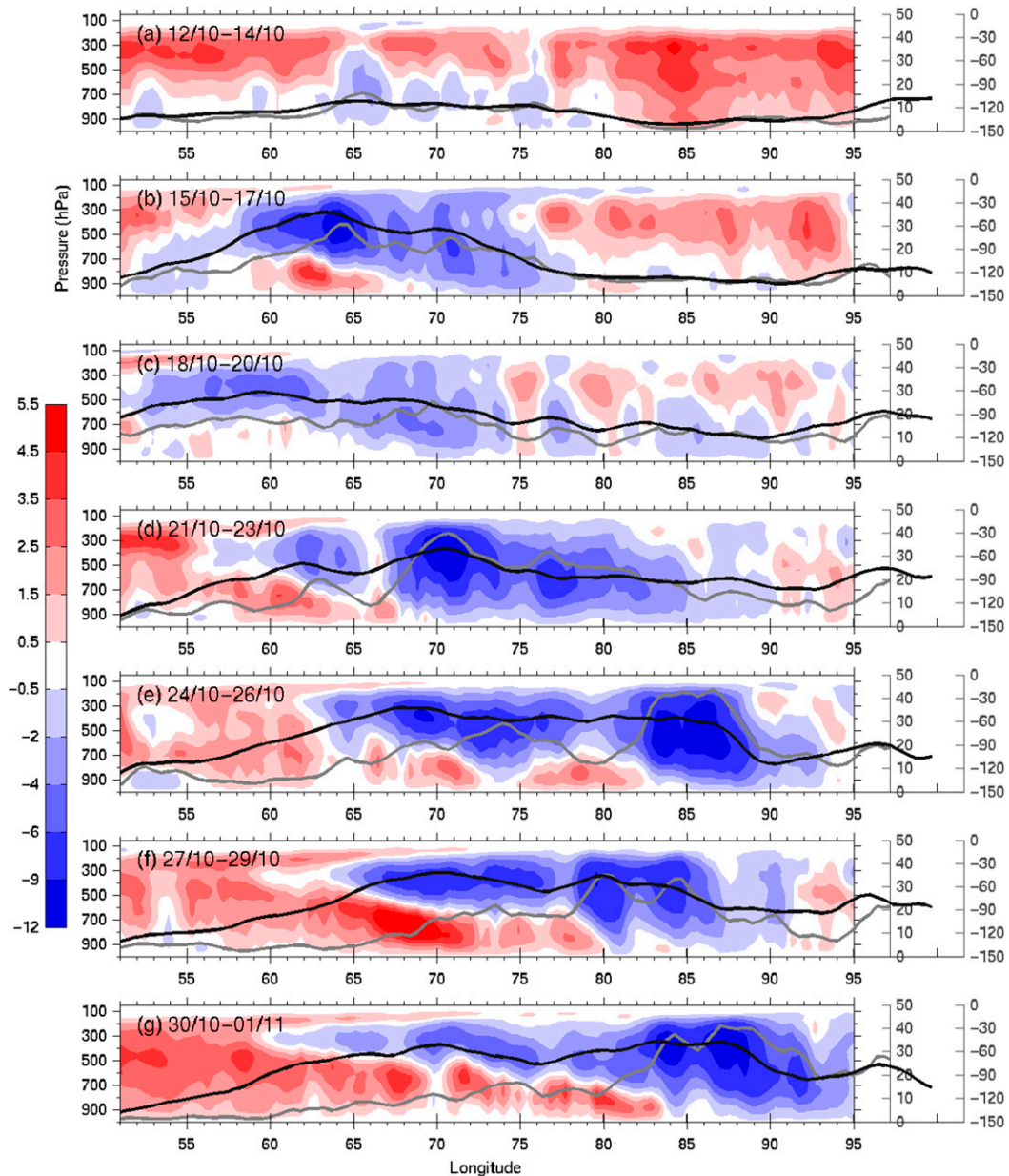
FIG. 4. Longitude–pressure diagram of 3-day-mean pressure velocity (hPa h^{-1}; red shading: descent; blue shading: ascent) from 12 Oct to 1 Nov, for the October MJO event. Surface rainfall (mm day^{-1}; gray curve with the vertical axis on the right) and column radiation (W m^{-2}; black curve with the vertical axis on the far right) are also shown. Omega, precipitation, and column radiation are first averaged over the latitudes 0°–5°N; a 250-km running average along longitude is also applied.

and low-wavenumber variability are not resolved well. The primary features standing above the background red spectrum are Kelvin waves and the westward inertia–gravity waves, bounded by the dispersion curves for the theoretical $n = 1$ inertia–gravity waves (WIGs) with equivalent depths between 12 and 50 m, corresponding to a phase speed of 10–22 m s^{-1} for WIGs with a horizontal wavelength in the range between 1000 and 1500 km. This

high-frequency wave activity is similar to the quasi-2-day waves observed during TOGA COARE (Takayabu et al. 1996).

b. Northward propagation of the two MJO events and tropical cyclones

In addition to the eastward propagation, both DYNAMO MJO events also have a slow northward propagation
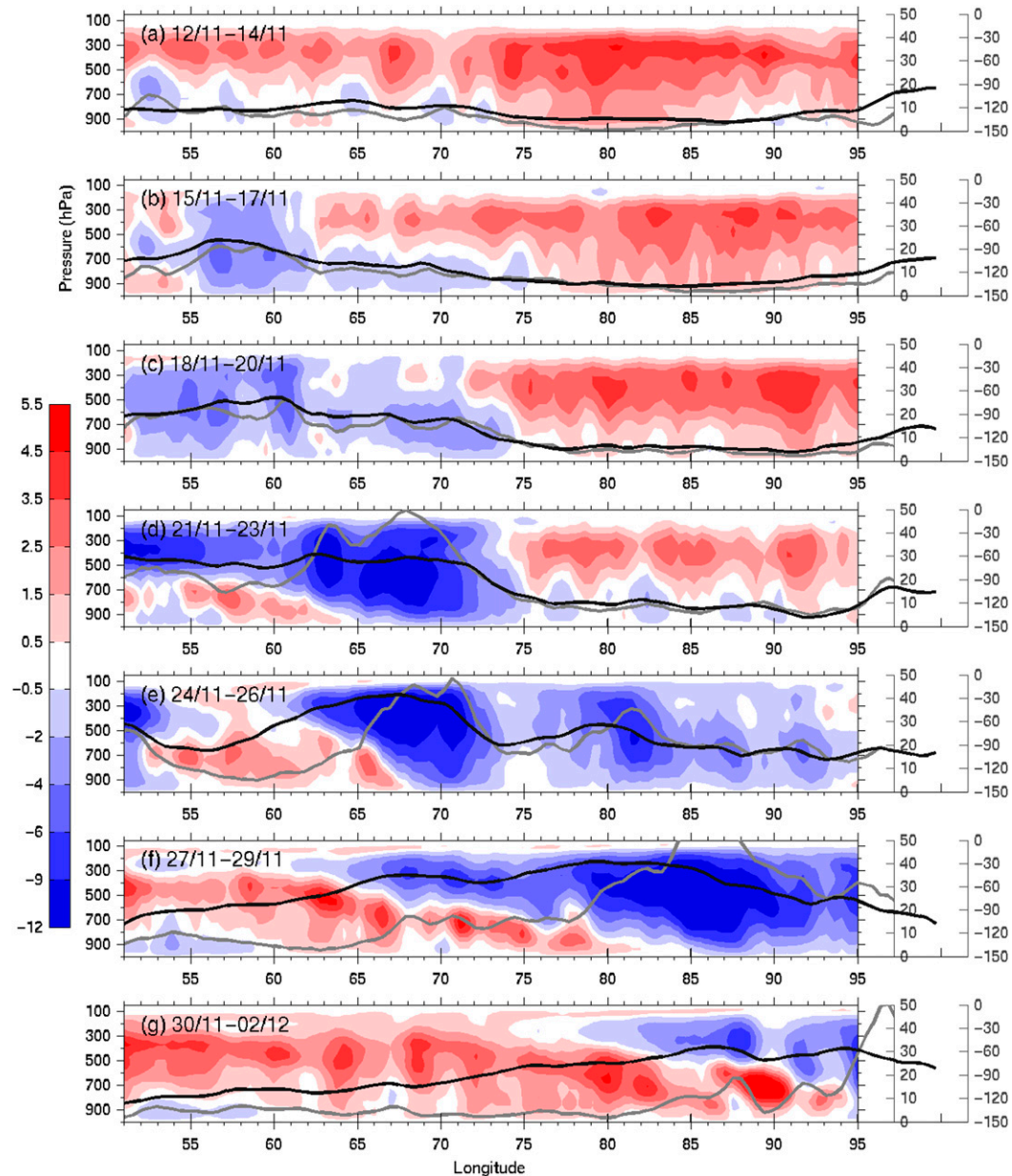
FIG. 5. As in Fig. 4, but from 11 Nov to 2 Dec for the November MJO event.

component. Figure 7 is a latitude–time diagram of daily precipitation and 850-hPa relative vorticity, both averaged between 55° and 90°E. The large-scale precipitation maxima migrate northward slowly, at a speed of ~1–2 m s^{-1}. For both model and observations, the precipitation signature of the October MJO event can be tracked to 15 October near 5°S. South of that latitude, persistent precipitation can be seen in TRMM, indicating the presence of the intertropical convergence zone (ITCZ) throughout the period. ITCZ precipitation is less persistent in the simulation.

Precipitation generally coincides with low-level cyclonic relative vorticity anomalies during the active MJO phases. These vortices are associated with "Rossby gyres" in the quasi-stationary response to heating (e.g., Gill 1980) but can evolve into tropical cyclones (TCs) in some events. Detailed synoptic analysis is needed to better understand the evolution of the disturbances in these specific events. Several vorticity plumes can be found north of 5°N and extending to the extratropics (e.g., in late October, early November, and late November) in both observations and the WRF simulation. These rotational
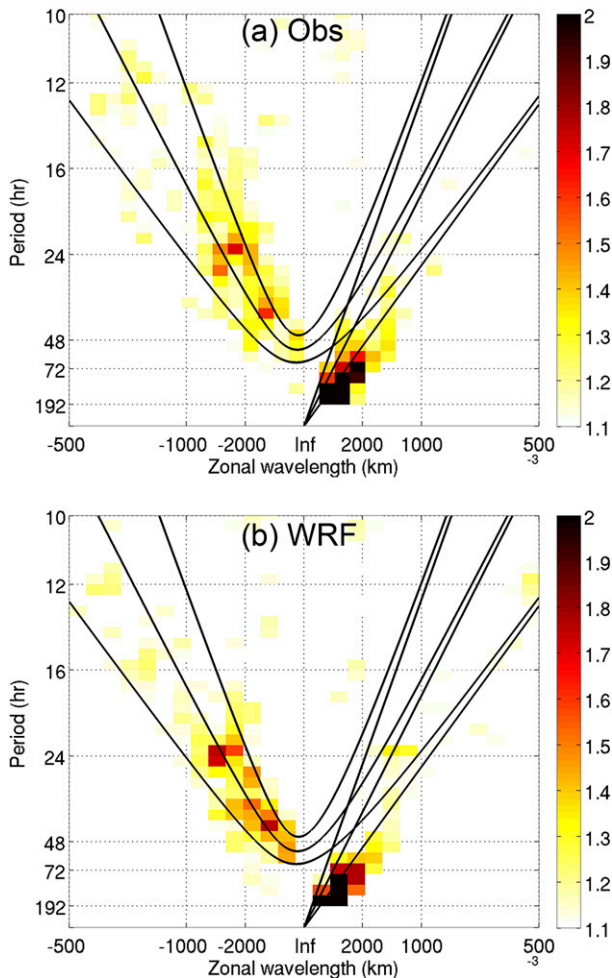
FIG. 6. Normalized spectrum of surface rainfall in the Indian Ocean (50°–90°E) averaged between 5°S and 5°N for (a) CMORPH and (b) WRF. The temporal window is 16 days, and the temporal resolution is every 3 h. The solid curve corresponds to $n = 1$ inertia–gravity waves and Kelvin waves with equivalent depths of 12, 25, and 50 m.

entities with local precipitation maxima are signatures of either tropical depressions or named tropical cyclones. We will refer to these features as tropical cyclones while not rigorously categorizing them into the intensity-based specific TC types, since the intensities simulated do not correspond closely to those in the observations. Perhaps because of our relatively low horizontal resolution (by the standards appropriate for representing TC dynamics), the simulation tends to produce weaker TCs than those observed.

Figures 8a–c show maps of total SSM/I precipitable water, TRMM rainfall, and ERA-Interim 850-hPa wind vectors at three dates close to those on which the vorticity plumes are best developed: 27 October, 3 November, and 27 November. The same variables from WRF are shown in Figs. 8d–f. On 27 October, while none of the best-track

data report even a tropical depression, strong low-level rotation and local precipitation maximum centered at 10°N, 62°E in the Arabian Sea indicate a TC-like structure. This is the remnant of an MJO Rossby gyre that migrated northwestward, bringing significant rainfall. In reality, this system continued to move toward the Arabian Peninsula, evolved into TC Keila (first named on 2 November), and struck the Oman coast as reported in the best-track record.

The 3 November event shown in Figs. 8b,e later developed to tropical storm 4 from 7 to 9 November in the western Arabian Sea, as reported in the Joint Typhoon Warning Center (JTWC) best-track dataset. The WRF also shows a TC-like structure at this day but simulates much less precipitation than is found in SSM/I. Nevertheless, the system shows a concentrated moisture anomaly along with precipitation and relative vorticity maxima.

The late November TC event, reported as tropical storm 5 (TC05A) in the JTWC best-track dataset, is sampled in Figs. 8c,f. This event was well forecast by several numerical models (e.g., Fu et al. 2013). On 27 November, the center of TC05A had reached around 12°N in the eastern Arabian Sea. At this time, WRF shows a rotational structure and axisymmetric rainfall distribution associated with the Rossby gyre, but it is larger and the center is located ~5°N, far south of that in the observations. Three days later, the WRF does show the axisymmetric TC structure having moved to ~12°N off the west coast of India. The delay of this TC event in the WRF simulation may be due to the delay of the simulated November MJO event, as discussed before and also shown in the time series of precipitation (Fig. 9).

Overall, the tropical cyclone events observed during the DYNAMO period appear to be closely related to the northward propagation of the two MJO events. Many days into the simulation, the WRF is still able to simulate the formation of TC-like events, although their intensities and tracks do not match observation exactly. These results are consistent with those of Vitart (2009) and Vitart et al. (2010) that show that improved simulation of the MJO can lead to more skillful TC forecasts on the intraseasonal time scale.

c. Comparison with the northern sounding array data

Johnson and Ciesielski (2013) show that the October and November MJO events maintain coherence in the northern sounding array region, while the occasional passage of synoptic-scale disturbances disrupts the MJO signals over the southern sounding array region. The present WRF configuration does not simulate each individual synoptic event in the southern sounding array well but produces a much better representation of the
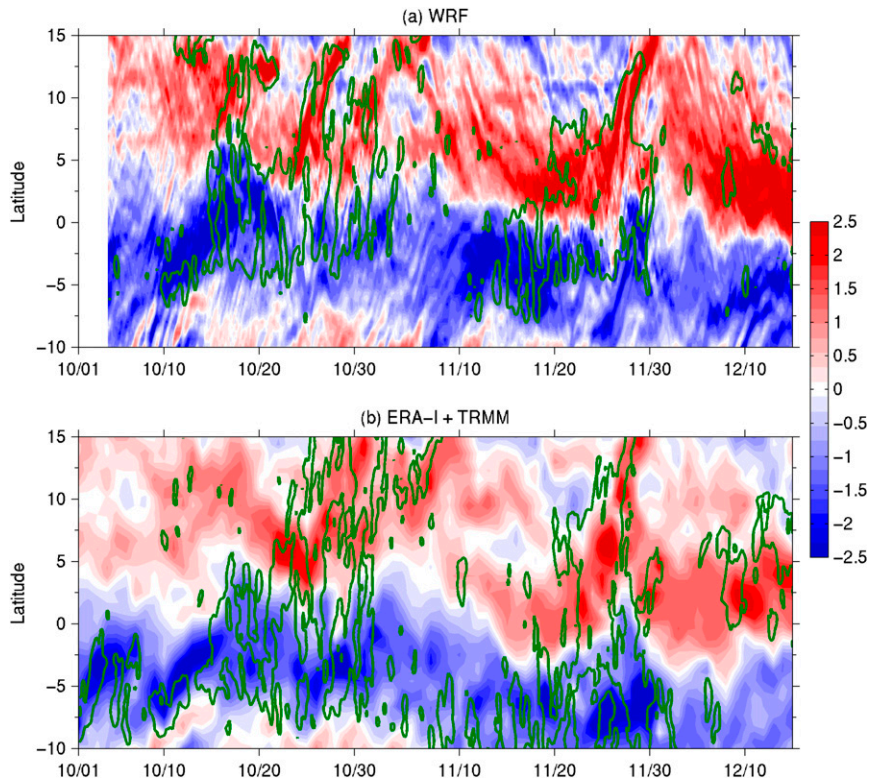
FIG. 7. Latitude–time diagram of relative vorticity at 850 hPa (shading; $10^{-5}\,\text{s}^{-1}$) and daily surface rainfall (green contour; $12\,\text{mm}\,\text{day}^{-1}$), both averaged in the longitude bands 55°–90°E.

large-scale MJO envelope. In the following, we compare the temporal evolution and vertical structure of various quantities from the model simulation in the NSA region against the sounding array observations.

Time series of outgoing longwave radiation (OLR) averaged over the region are shown in Fig. 9. CERES top-of-atmosphere (TOA) OLR shows a significant reduction from ~290 to $180\,\text{W}\,\text{m}^{-2}$ (i.e., by ~$100\,\text{W}\,\text{m}^{-2}$) during the October MJO event and by ~$150\,\text{W}\,\text{m}^{-2}$ during late November. Reflected shortwave radiation (RSW) at TOA shows a significant increase from $50\,\text{W}\,\text{m}^{-2}$ in the suppressed phase to more than $200\,\text{W}\,\text{m}^{-2}$ in the active phase. This dramatic reduction in both OLR and downward shortwave is a marked feature of the MJO events in the Indian Ocean. The radiation anomalies may lead to radiative–convective instability, as several authors have postulated may be important to the MJO (Lee et al. 2001; Raymond 2001; Bony and Emanuel 2005; Sobel et al. 2008). The simulated OLR anomaly during late October and November is about $10\,\text{W}\,\text{m}^{-2}$ less than CERES at the peak of the MJO convective phases. The reflected shortwave radiation at the top of the atmosphere (Fig. 9c) is $10\,\text{W}\,\text{m}^{-2}$ less than CERES. At TOA the longwave and shortwave compensate each other to a great degree in both CERES and the simulation. Net

column radiative heating will be further discussed later in the context of the atmospheric moist static energy budget.

The vertical structures of the large-scale vertical motion, zonal winds, temperature, and humidity fields are shown in Fig. 10, and their time means and standard deviations are shown in Fig. 11. The large-scale vertical motion (W) derived from the NSA horizontal winds using mass conservation (Johnson and Ciesielski 2013) (Fig. 10b) shows multiple episodes of ascent in the October MJO events and two strong such episodes in the November events. The WRF simulation shows similar behavior. Vertical motion in both the model and NSA sounding data has a first baroclinic mode structure during the MJO active phase followed by the development of a top-heavy second baroclinic mode structure though somewhat more so in the simulation than in the observations. This time progression also resembles the time–longitude diagram in Figs. 3 and 4.

The simulation differs from the sounding array data in several aspects: as with precipitation, the maximum in W is larger in the simulation than in the observations for the October event but weaker for the November event. The time-averaged vertical profile of W from the NSA is top heavy, similar to W from the TOGA COARE in the
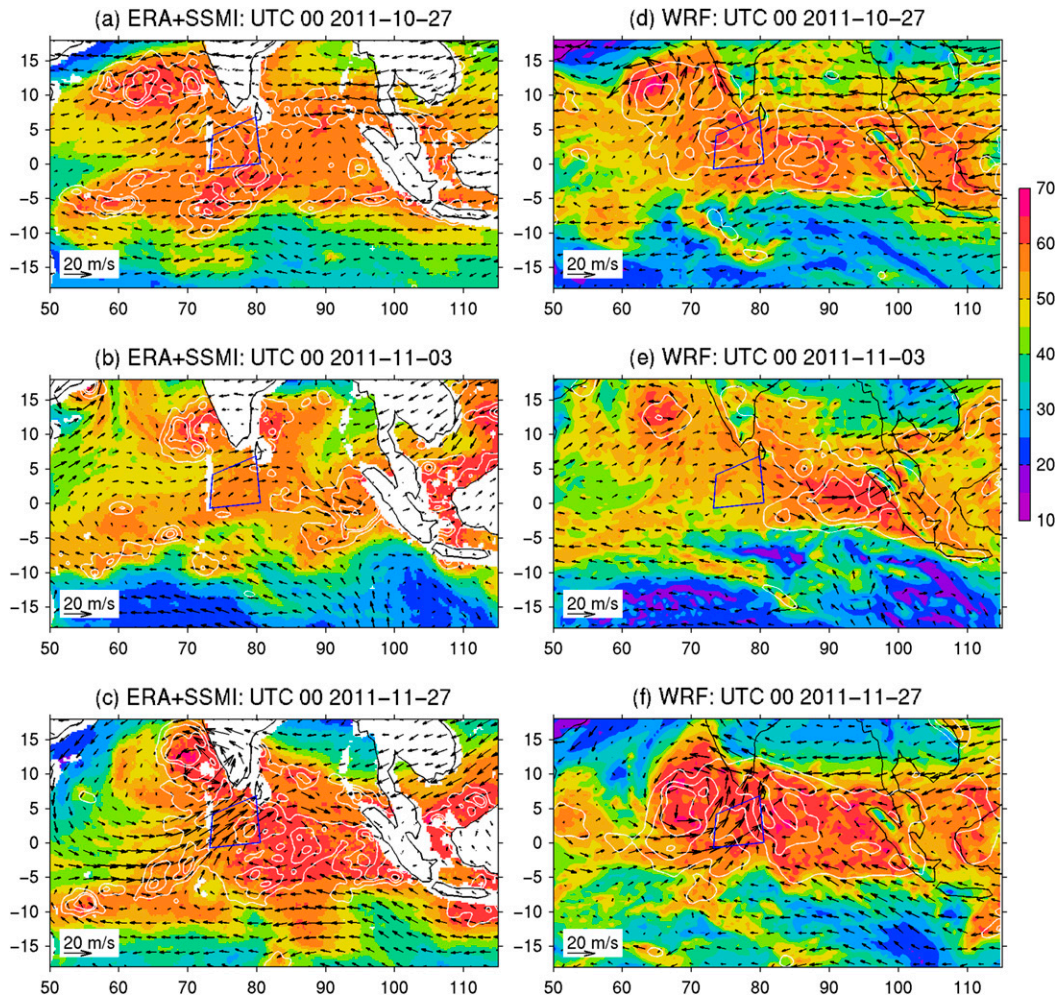
FIG. 8. (left) Total precipitable water from TMI and SSM/I (shaded), TRMM daily precipitation (white; 10, 30, and 50 mm day^{-1}), and ERA-Interim horizontal winds at 850 hPa (vectors). (right) As in (left), but for the WRF simulation. Three time snapshots are shown: (top) 0000 UTC 27 Oct, (middle) 0000 UTC 3 Nov, and (bottom) 0000 UTC 27 Nov.

western Pacific, with a peak value of $\sim$1.2 cm s^{-1}. The WRF-simulated mean values of W agree well with the observations (Fig. 11a) but with an upper-tropospheric peak at slightly lower altitude ($\sim$400 hPa) and slightly weaker amplitude. The standard deviation (Fig. 11b) also shows similar vertical structure with a local maximum in the upper troposphere.

The low-level westerly wind burst is one of the defining characteristics of the MJO (e.g., Lin and Johnson 1996). Figures 10c,d compare the model-simulated zonal wind and that from the NSA. During the first half of October, the wind in the lower troposphere (600–800 hPa) over the NSA is dominantly westerly, becomes easterly prior to the October MJO event, and turns back to westerlies during the MJO active phase (late October and early November). After the rainfall peak in the last 2 weeks of October, the westerlies continue to

strengthen until the middle of November. The simulated transition from easterly to westerly in the lower troposphere starts from near the surface around 20 October and then deepens, reaching 400 hPa in the first week of November, while the observations show a similar but less distinct gradual deepening of the westerly over a $\sim$5-day period near 1 November. During this period of westerly development, the upper-tropospheric easterlies also strengthen. After the passage of the October MJO event, easterlies prevail in both model and observations until around 20 November, when the November MJO event arrives at the NSA. The lower-tropospheric westerly wind burst is nearly 10 m s^{-1} in observations and greater than 10 m s^{-1} in the model. The NSA region remains westerly until the middle of December. The averaged zonal wind profile features a peak of 10 m s^{-1} easterly wind at $\sim$200 hPa, with weak westerlies in the
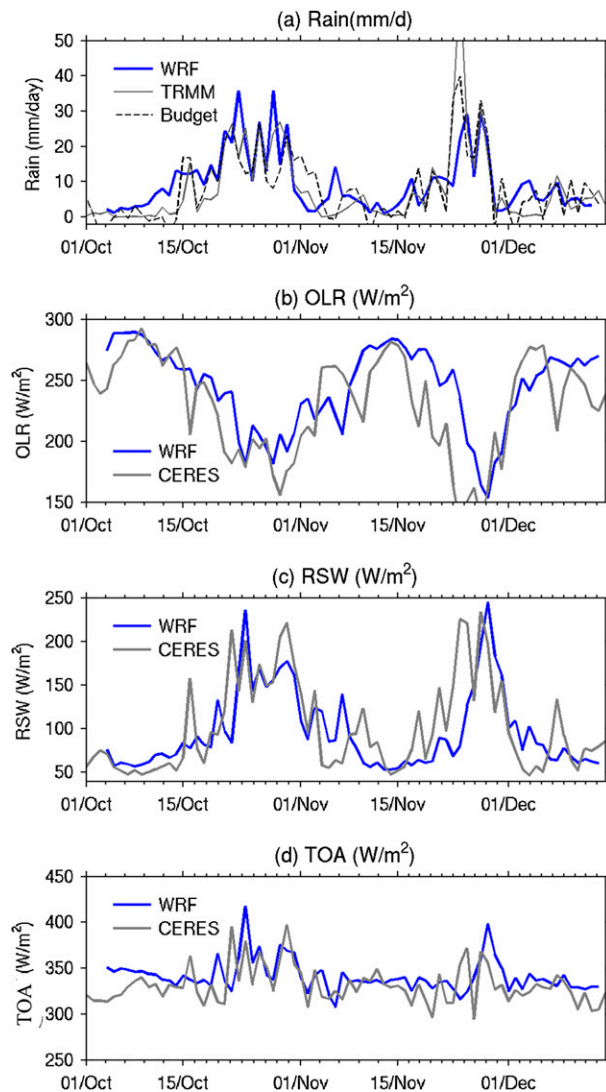
FIG. 9. Time series of (a) precipitation (mm day^{-1}) from WRF, TRMM, and budget-derived rainfall; (b) OLR (W m^{-2}) from WRF and CERES; (c) reflective shortwave radiation; and (d) net top-of-atmosphere radiation averaged over the NSA region. Quantities from WRF are averaged over the region 0°–5°N, 73°–80°E.

lower troposphere, as seen in both model and observations (Fig. 11c). The standard deviation (Fig. 11d) has a peak at ~150 hPa in both model and observations, but the model's standard deviation is larger from 900 to 400 hPa.

Figures 10e,f compare the vertical structure of temperature anomalies, computed by subtracting the time mean of temperature profiles spatially averaged over the NSA. A positive temperature anomaly can be seen through the depth of the troposphere from 10 to 15 October and persists in the upper troposphere during the MJO active phase (the last two weeks of October). A negative temperature anomaly is first found in the lower

troposphere during the last two weeks of October, while the lower-tropospheric westerlies are still weak. Afterward, the negative temperature anomalies continue to extend to the upper troposphere and show a tilted structure in the time–height plot with a minimum in the 200–400-hPa layer. The tilted positive temperature anomaly prior to the MJO rainfall peak and the negative temperature anomaly after it, as described for the October event, are also seen for the simulated November MJO event, though evolving at a faster pace. The same structural evolution is seen in the sounding array observations but somewhat less coherently. There is also significant temperature variability near the tropopause (100–150 hPa), which is likely due to vertical propagation of Kelvin waves or inertia–gravity waves. The simulated temperature anomalies generally agree well with observations in the vertical structure of standard deviation (Fig. 12d).

Figures 10g,h show relative humidity with respect to ice, computed from the profiles of temperature and water vapor averaged over the NSA. The dryness of the troposphere during the suppressed MJO phase is evident in both WRF simulation and NSA observations. Gradual lower-tropospheric moistening occurs prior to the MJO events (10–20 October and 15–20 November), when the low-level wind is easterly (Figs. 10c,d) and the temperature anomaly is positive (Figs. 10e,f). The subsequent drying after the active phases is less dramatic in the WRF simulation than in observations for the November event. The time-mean relative humidity also shows a local maximum near the tropopause, between 100 and 200 hPa (Fig. 11g), ~80% in NSA and 60% in WRF. This local peak also persists during the suppressed MJO phase. This feature may be related to the anomalous cirrus activity found in MJO composites of satellite observations (e.g., Virts and Wallace 2010; Del Genio et al. 2012). A local maximum is also seen in the standard deviation of relative humidity in NSA, but it is much weaker in WRF. The reduced variation in relative humidity between 100 and 200 hPa in WRF indicates that WRF has difficulty in capturing variability associated cirrus near the tropopause.

In short, comparison with observations in the northern sounding array indicates that the WRF simulation captures the passage of two MJO events over the NSA region with high fidelity. A prominent feature from this analysis is that the lower troposphere leads the upper troposphere in nearly all variables (vertical velocity, moisture, temperature anomaly, and zonal wind), indicating a westward tilt spatial structure during the two MJO life cycles. This spatial tilt agrees with what is seen in MJO composites (e.g., Kiladis et al. 2005) in some variables (zonal wind, temperature, and humidity), suggesting they
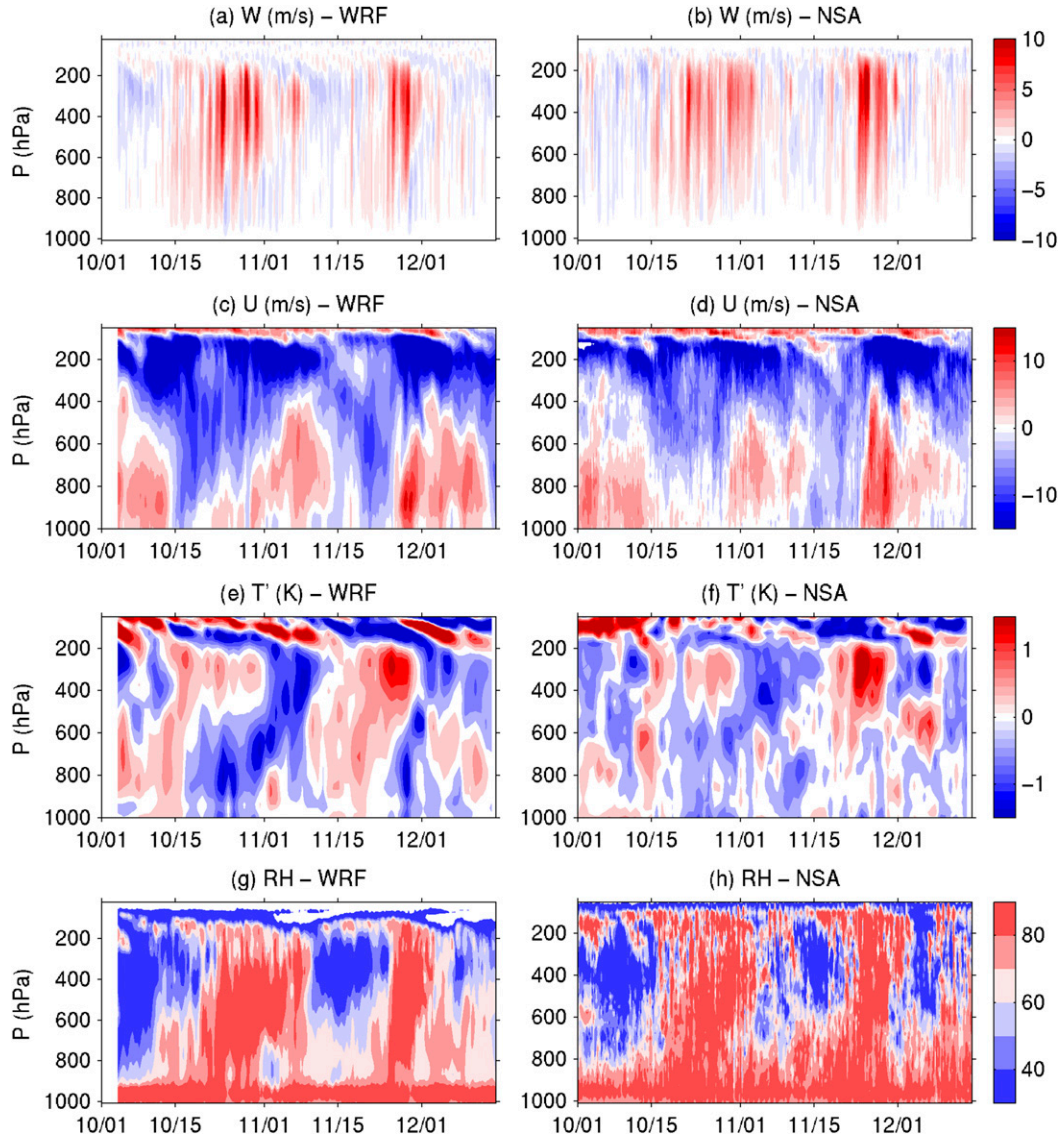
FIG. 10. Vertical motion (cm s^{-1}) from (a) WRF averaged over the region 0°–5°N, 73°–80°E and (b) the DYNAMO northern sounding array. (c),(d) As in (a),(b), but for zonal winds (m s^{-1}). (e),(f), As in (a),(b), but for temperature anomaly (K). (g),(h) As in (a),(b), but for relative humidity (%).

are not case specific but are general enough to be considered as a common feature of MJO events. In the following, we continue to analyze these MJO events in the NSA region, with a focus on quantification of the moisture and moist static budgets.

d. The role of time-varying SST

In this section, we assess the role of the imposed time variations in SST on the simulated MJO events. It may be argued that, since the MJO is to some extent a coupled atmosphere–ocean phenomenon, imposing daily SST is inappropriate and a coupled modeling approach is superior (e.g., Seo et al. 2014). While a coupled model

is clearly a more comprehensive representation of the real climate system, the appropriate model configuration may depend on the objectives of the study. Our simulations already incorporate time-varying lateral boundary conditions which are influenced by atmospheric observations from outside the domain. That exterior atmosphere is coupled to the atmosphere within the domain as much as the SST within the domain is; there is no fundamental difference between specifying these lateral boundary conditions and specifying the SST as a lower boundary condition. These are not forecast model runs, as those assessed in Ling et al. (2014), but simulations designed to produce a set of three-dimensional atmospheric fields that
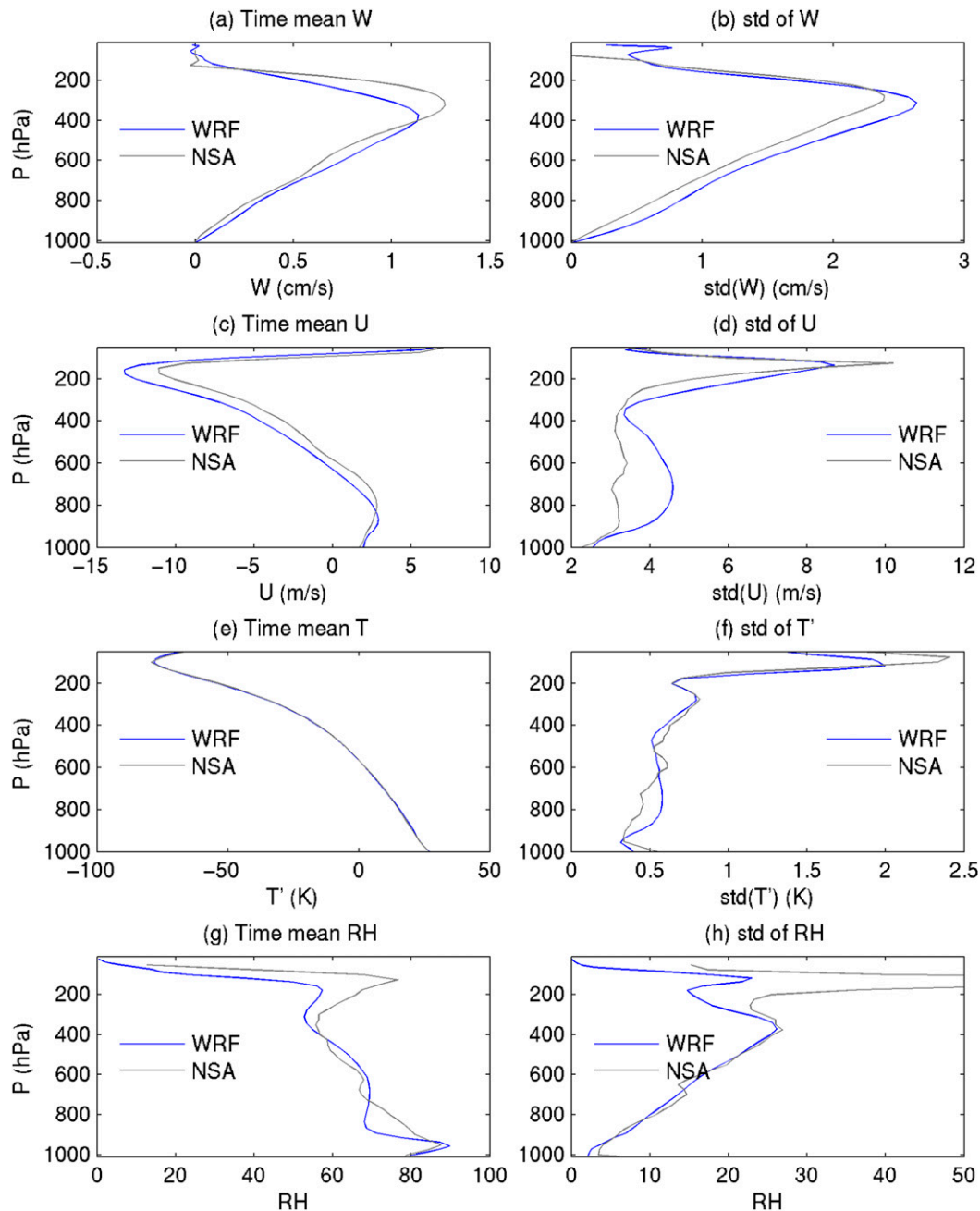
FIG. 11. Time mean and standard deviation of vertical velocity, zonal winds, temperature, and relative humidity from (left) WRF over the region 0°–5°N, 73°–80°E and (right) the DYNAMO northern sounding array.

are both internally consistent within the atmosphere (given the model dynamics, physics and numerics) and as consistent as possible with the observed atmospheric evolution during the simulation period. The observed daily SST, like the lateral boundary conditions, is a mathematically well-posed condition to help achieve consistency with observations.

It is nonetheless of interest to know how strongly the daily SST influences the simulated MJO events. We

investigate this by conducting a numerical experiment in which daily SST is replaced by time-independent SST averaged from October to the end of December. Figure 12b shows the 850-hPa zonal winds and surface precipitation from this experiment. The October MJO event is reasonably well reproduced in these two variables with time-independent SST, although the MJO signature is weaker and its eastward propagation is faster. For the November MJO event, the MJO can
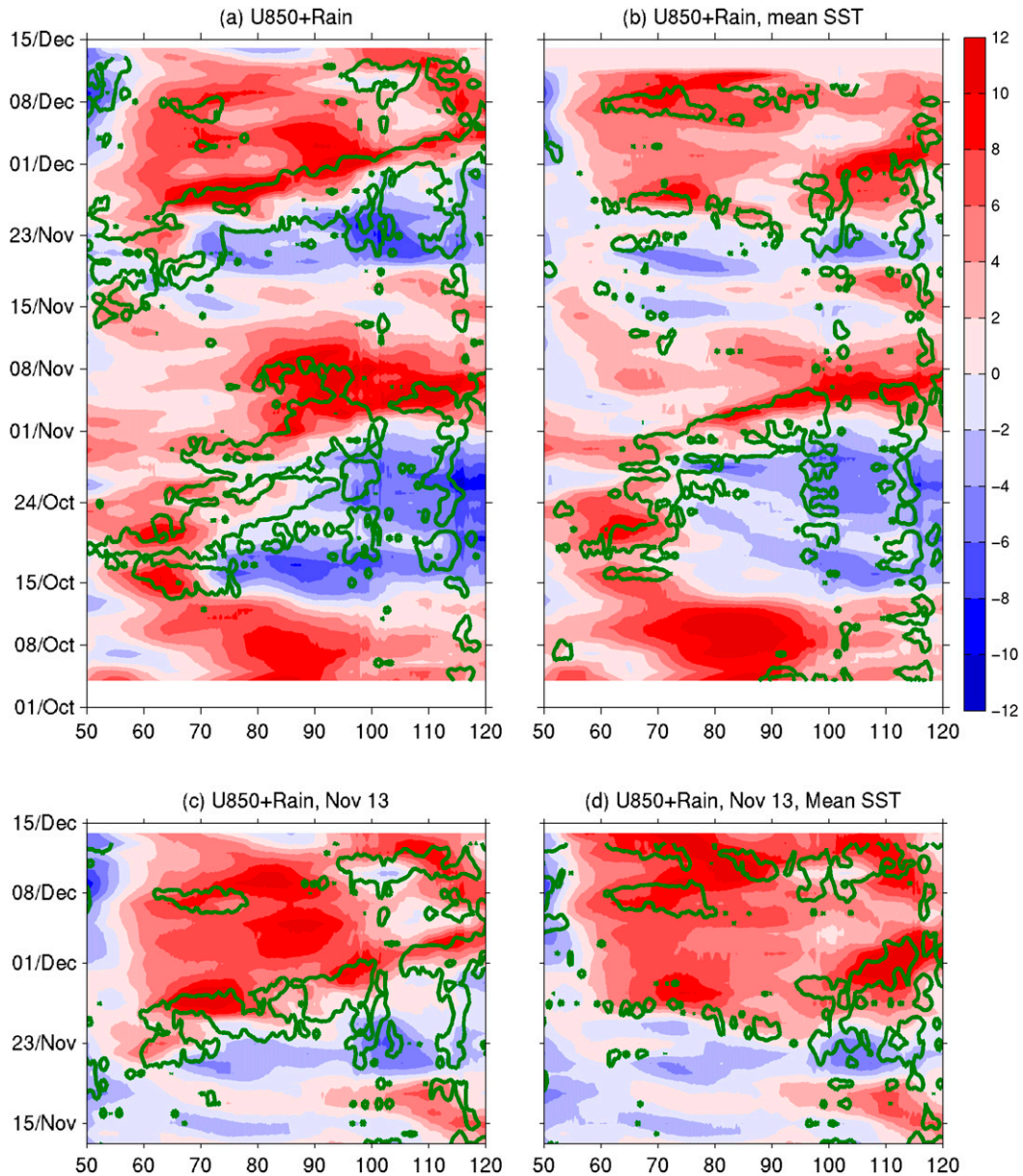
FIG. 12. (a) Precipitation (15 mm day^{-1}) and 850-hPa zonal wind averaged between the equator and 5°N from daily SST (identical to Fig. 3a). (b) Time-independent SST averaged from October to December. (c) As in (a), but initialized on 10 Nov. (d) As in (c), but with time-independent SST averaged from 13 Nov to 13 Dec.

barely maintain its strength. Thus, this experiment seems to indicate that daily SST plays different roles in the two MJO events: it is more important in the November event than in the October event.

However, the November MJO event occurs later in the simulation, so it is possible that the inferior simulation of it compared to the October event could be a consequence of the drift of the model solution away from the observed atmospheric state, rather than any inherent difference between the two MJO events. To address this issue, we

perform another pair of simulations initialized at 0000 UTC 10 November with horizontal winds nudged toward reanalysis (as described in the last paragraph of section 2a) until 0000 UTC 13 November. These two otherwise identical simulations differ in one aspect: one uses daily SST and the other uses monthly-mean SST. Results from these two simulations (Figs. 12c,d) differ substantially: the November MJO event is well reproduced in the daily SST event but poorly simulated with monthly-mean SST. This is similar to the results from the

two experiments initialized from 1 October (Figs. 12a,b). Together, these two pair experiments suggest that daily SST plays an important role for the November MJO event but much less so for the October event. This result is consistent with Fu et al. (2015), who demonstrated that the role of SST anomalies varies from event to event based on observation and global modeling experiments. A deeper understanding of this difference between the two events will require further research.

4. Budgets of water vapor and moist static energy

The moist static energy (MSE) budget of the MJO has been explored in both observations and simulations (e.g., Maloney 2009; Raymond and Fuchs 2009; Maloney et al. 2010; Kiranmayi and Maloney 2011; Wu and Deng 2013; Andersen and Kuang 2012; Mapes and Bacmeister 2012; Kim et al. 2014). S14 recently constructed the MSE budget of the DYNAMO MJO events studied here using both observation and the ERA-Interim reanalysis data in the NSA region and showed that both the large-scale horizontal and vertical advection term had a negative contribution to the MSE budget during the active phases. We will examine the budget in our simulations and compare them to observations in this section.

a. Budget of water vapor

We first consider the column-integrated budget of water vapor, which has also been used to study the MJO by some authors (e.g., Hsu and Li 2012). It is written as

$$\left\langle \frac{\partial q_v}{\partial t} \right\rangle = \text{HADV}_q + \text{VADV}_q + E - P, \quad (1)$$

$$\text{HADV}_q = -\langle \mathbf{v}_h \cdot \nabla q_v \rangle, \quad \text{and} \quad \text{VADV}_q = -\left\langle \omega \frac{\partial q_v}{\partial p} \right\rangle,$$

where $\mathbf{v}_h$ is the horizontal wind vector, $\langle \ \rangle$ denotes a mass weighted vertical integral, $\langle \ \rangle = \int_0^1 \mu \, d\eta/G$, μ is the total dry mass, η is vertical coordinate of WRF, HADV_q and VADV_q are horizontal and vertical advection at resolved scales by the model, E is surface evaporation, and P is precipitation. The vertical integral is effectively taken from the surface to ~20 hPa, the pressure of the topmost model layer. Note that we have neglected the diffusion process, which smooths out the moisture field; therefore, it is not a source/sink in a global domain but it may still be a net source/sink at local area. As shown below, the rhs and lhs of Eq. (1) agree quite well, indicating that this omission in Eq. (1) is justified. The two nonlinear advection terms at the resolved scales are evaluated using variables averaged over 7 adjacent grid cells. Skamarock (2004) demonstrated that 6–7 times the model horizontal grid spacing (63 km) is the effective
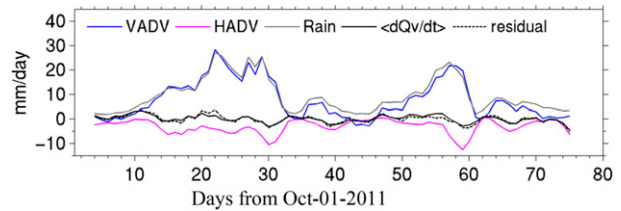

FIG. 13. Column-integrated water vapor budget over the NSA regions (0°–5°N, 73°–80°E): vertical advection (blue), horizontal advection (magenta), rain (gray), residual of the rhs of Eq. (1) (dotted), and the tendency term (black). A 3-day moving average is applied to all the time series.

scale above which numerical diffusion is considered to be unimportant for kinetic energy.

Figure 13 shows the moisture budget over NSA at 3-hourly temporal sampling. The dominant terms are vertical advection and rain, as expected, and the horizontal advection is ~10 mm day^{-1} during the active phase, similar to what is computed from the sounding array budget (Johnson and Ciesielski 2013). S14 and Kerns and Chen (2013) demonstrated that horizontal advection plays a significant role in the observed MJO events. Surface evaporation is smaller than any of these three terms and is not shown here. The role of shallow and deep convection in the moistening may also be deduced by comparing Fig. 13 with the vertical structure of large-scale vertical motion. The moistening of the lower troposphere around 10–20 October (Fig. 10), when rainfall does not exceed 15 mm day^{-1}, can be attributed to vertical advection associated with the shallow circulation (Figs. 4a–c), while vertical moisture transport due to deep convection and stratiform processes (Figs. 4d–f) dominates the moisture budget during the heavily raining period of 20–30 October. The agreement between the directly computed local change of column-integrated water vapor on the left-hand side of Eq. (1) and the total tendency terms (all the right-hand side terms) is good despite the relatively coarse temporal resolution in this calculation.

b. Budget of moist static energy

The column-integrated budget for MSE may be written as

$$\left\langle \frac{\partial e}{\partial t} \right\rangle = \text{HADV}_e + \text{VADV}_h + R + \text{SH} + \text{LH} + D_h, \quad (2)$$

where e and h represent frozen moist enthalpy ($e = c_p T + L_v q_v - L_f q_i$, where q_v is water vapor and q_i is ice) and frozen moist static energy ($h = e + gz$), respectively. The term R refers to column net radiation, SH refers to surface sensible flux, LH refers to surface latent flux, and D_h refers to subgrid diffusion and numerical diffusion. The left-hand side is the
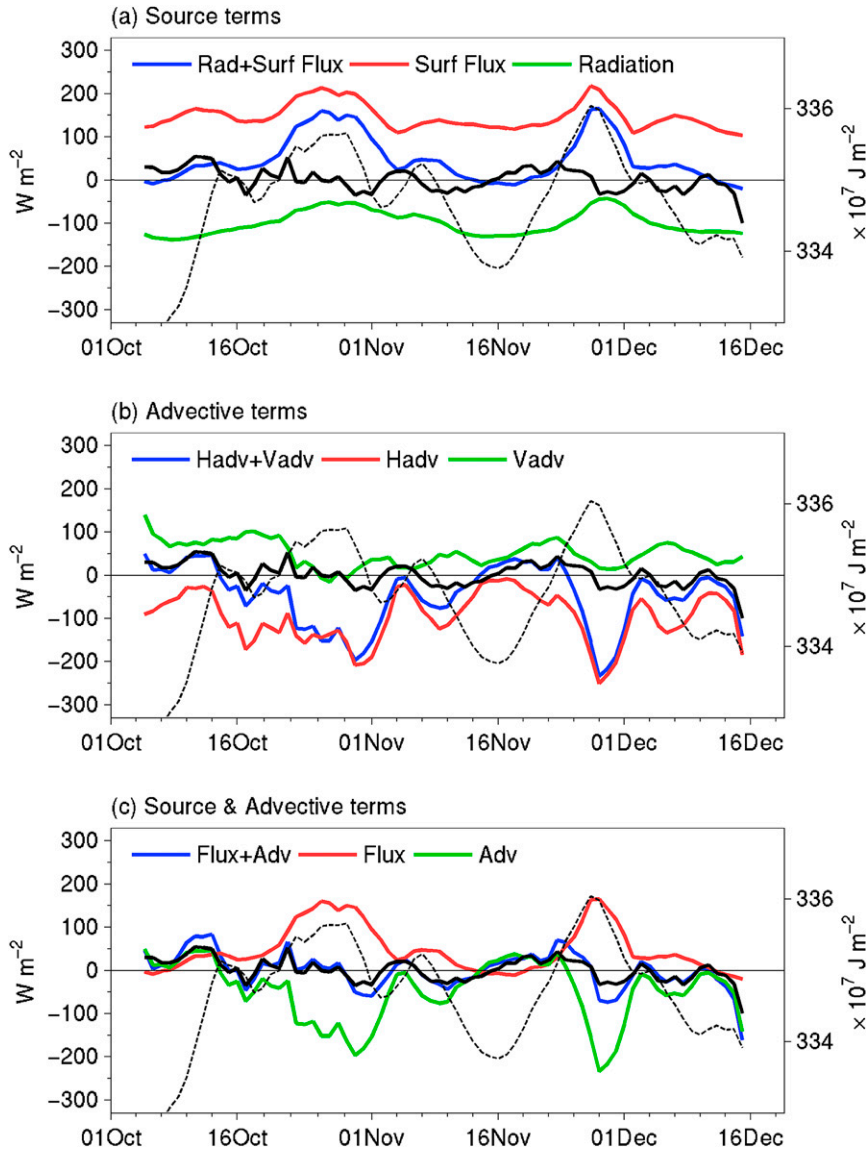
FIG. 14. Time series of various budget terms of moist static energy over the NSA region: (a) radiation and surface fluxes; (b) horizontal and vertical advection; and (c) sum of these terms (blue) and the directly estimated tendency $\langle \partial \mathrm{MSE}/\partial t \rangle$ (black). Simulated MSE (dashed) is also shown to indicate MJO events.

column-integrated local tendency of frozen moist enthalpy, which will also be referred as the storage term. The term VADV_h is the vertical integral of vertical advection of moist static energy, and HADV_e is the vertical integral of the horizontal advection of moist enthalpy. Together, these two terms will be referred as advection terms in the MSE budget, while $R + \mathrm{SH} + \mathrm{LH}$ will be referred to as the diabatic terms. [The "diabatic heating" that would appear in a potential temperature or dry static energy equation because of condensation of water vapor is not present in Eq. (2) because MSE is conserved under phase change of water.] The conversion from kinetic energy to potential energy, although small, is accounted in HADV_e, following Eq. (10.3) in Neelin (2007). The diffusion term is typically neglected. Validity of the MSE Eq. (2) seems to be questionable for nonhydrostatic processes simulated in the WRF, since the MSE equation is strictly valid in the hydrostatic limit. However, it is still appropriate at least for horizontal length scales significantly larger than the depth of the troposphere (here comparable to our horizontal grid spacing), at which nonhydrostatic effects are small.

Figure 14 shows the column-integrated MSE budget, including vertical and horizontal advection, surface

fluxes, column net radiative fluxes, and the storage term, all averaged over the region of the NSA. The surface enthalpy fluxes and radiation terms are computed as the averages of direct model output. Figure 14a shows these diabatic terms and their sum. Both terms increase during the onset of the MJO phases. This result agrees with observations for the November MJO event in that both surface fluxes and radiation contribute to the buildup of the MSE anomalies (S14). However, the large-scale surface fluxes from the observation (Fig. 3 of S14) remain nearly constant during the October MJO event, while the WRF simulation shows a dramatic increase of surface fluxes in the middle of October.

The advection terms in the MSE budget are shown in Fig. 14b. The horizontal advection $HADV_e$ is close to $200\,\mathrm{W\,m^{-2}}$ in the active phase, larger than that derived from either the sounding network or the ERA-Interim dataset (on the order of $100\,\mathrm{W\,m^{-2}}$ during the MJO active phases; see Fig. 3 and 4 of S14). Vertical advection is positive ~10 days before MSE peaks because of shallow circulation, becomes negative after the MJO onset for the October MJO, and reaches the minimum after the MSE peaks, similar to that in observations (S14). The sum of $HADV_e$ and $VADV_h$ (Fig. 14c) shows a broader period of positive values before the MSE peaks, contributed by advection terms 5–10 days before the rainfall peak and by the diabatic terms within a few days before rainfall peak, becoming negative as the MJO active phase moves out of the NSA region. The different contribution of advection and diabatic terms at different lead times relative to the rainfall peaks is also observed from the budgets derived from the sounding array (S14).

There is a strong cancellation between the diabatic terms (blue) and the advection terms (red). The sum of all the tendency terms excluding diffusion (Fig. 14c) is in some qualitative respects similar to the advection terms alone throughout the entire period but more positive immediately before rainfall peaks because of the positive contribution of the diabatic terms. The agreement between the local change of column-integrated MSE and the sum of the all tendency terms (excluding diffusion) is overall quite good. In fact, difference in the time mean of the lhs and rhs excluding diffusion of Eq. (2) is only 1–2 W m^{-2}, as also discussed below.

The time-averaged values of the MSE budget terms may also be compared to those derived from observations. The time-mean vertical and horizontal advections of MSE derived from the sounding array are -23 and $-26\,\mathrm{W\,m^{-2}}$, respectively, while those from WRF are 50 and $-100\,\mathrm{W\,m^{-2}}$, respectively. The sum of the advection terms, on the other hand, is $\sim-50\,\mathrm{W\,m^{-2}}$ from WRF, which agrees well with that from the sounding array ($-49\,\mathrm{W\,m^{-2}}$). This agreement appears to be due to cancellation between

the vertical and horizontal advection terms. In the simulation, the time-averaged surface flux is $147\,\mathrm{W\,m^{-2}}$ and column-integrated radiative heating is $-100\,\mathrm{W\,m^{-2}}$, while the net surface flux is $111\,\mathrm{W\,m^{-2}}$ from the OAFlux observational product (used in S14) and the column radiative heating derived from CERES is $-72\,\mathrm{W\,m^{-2}}$.

c. NGMS

The import or export of MSE by large-scale advection can be expressed in terms of the gross moist stability (Neelin and Held 1987; Raymond et al. 2009), which plays a key role in the dynamics of moisture modes. Raymond and Fuchs (2009) suggest that a negative normalized gross moist stability (NGMS; column-integrated moist static energy import in the presence of moisture convergence) is a general feature in the Indian Ocean. Several authors have analyzed the NGMS in climate simulations and found that NGMS is a useful diagnostic for differentiating models that have better representations of the MJO, although persistent model biases complicate interpretation (e.g., Benedict et al. 2014).

The NGMS is normally difficult to estimate from observations, because of the difficulty of deriving large-scale vertical motion with sufficient accuracy from observational datasets. S14 derived the temporal evolution of NGMS within the MJO life cycles from the sounding network observational dataset (Johnson and Ciesielski 2013). They showed that the NGMS takes small positive or even negative values during the onset of the MJO active phase and then increases to relatively large positive values late in the active phase.

Figure 15 shows time series of NGMS, defined here as

$$\mathrm{NGMS} = \frac{\langle \mathbf{v}_h \cdot \nabla e \rangle + \left\langle \omega \dfrac{\partial h}{\partial p} \right\rangle}{\left\langle \omega \dfrac{\partial s}{\partial p} \right\rangle}, \tag{3}$$

from the WRF simulation. The denominator and numerator are advection terms in the moist and dry static energy budgets, respectively; therefore, they may also be computed via the residual terms in the budget equation. The estimate of NGMS indirectly from the residual terms will be referred to here as the indirect estimate of NGMS, while the NGMS computed using Eq. (3) will be referred to as direct NGMS. It can be shown by rearranging the dry and moist static energy budgets that NGMS is directly related to precipitation in the time mean: small or even negative NGMS is generally associated with large precipitation (Sobel 2007; Raymond et al. 2009; Wang and Sobel 2011, 2012; Wang et al. 2013; Anber et al. 2014). The following procedure is used to estimate NGMS: All variables are averaged to the
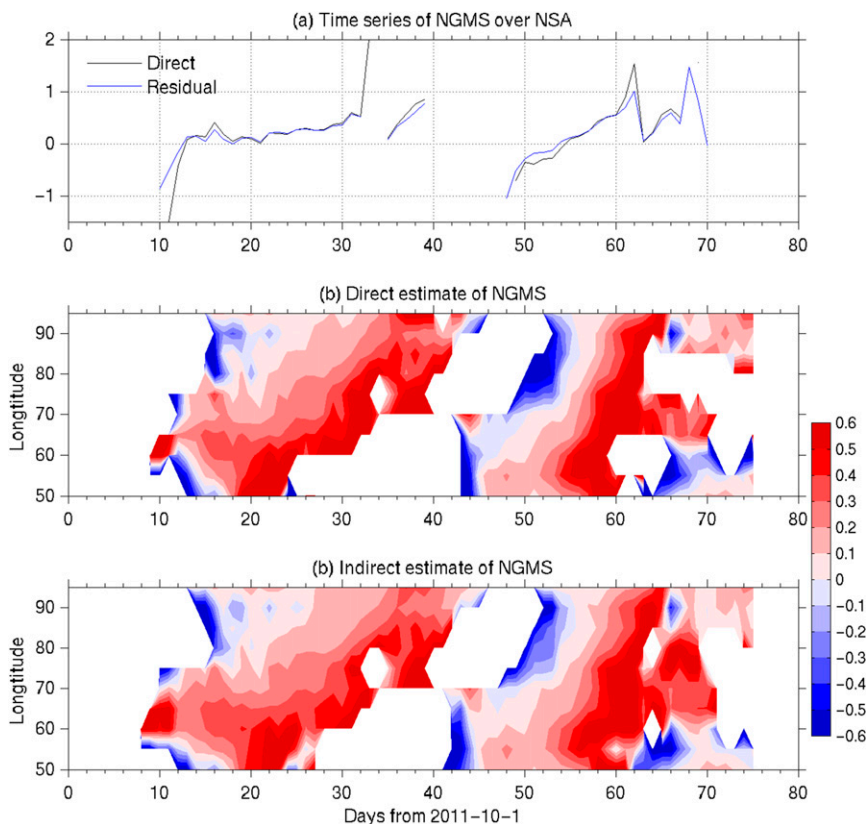
FIG. 15. (a) Time series of normalized gross moist stability. (b) Time–longitude diagram of directly estimated NGMS. (c) As in (b), but for indirectly estimated NGMS computed using the MSE budget. NGMS is not shown when the denominator is less than $1/5$ of its time-mean value.

effective model resolution (63 km). Spatial averaging and temporal averaging are applied to the denominator and numerator before we evaluate NGMS. Specifically, they are averaged over the NSA region and further smoothed by a 5-day running average. The estimate of NGMS is meaningless if the denominator gets close to zero and/or changes sign; for this reason, we do not show NMGS when the denominator is smaller than the average value of the denominator, as in S14. The NMGS during much of the suppressed phase is omitted as a consequence.

As in the observation analysis in S14, NGMS in the NSA region from the WRF simulation is negative before the precipitation peak and increases gradually to 0.8 at a later stage (Fig. 15a). The temporal evolution of NGMS reflects the transition of the large-scale vertical motion from shallow and bottom heavy to deep convection regimes and top-heavy omega profiles, as also shown in Figs. 4 and 5 for both MJO events. The agreement between direct and indirect estimated NGMS lend us some confidence in our estimate of NGMS.

Figures 15b,c show the longitudinal variation of the time series of both directly and indirectly estimated NGMS. The denominators and numerators are estimated

at the spatial resolution of 5° within the latitude belt from the equator to 5°N. Values of NGMS less than −0.6 are seen at nearly all longitudes, followed by gradual increases of NGMS to positive values, except around 10 October at 60°–70°E. Nevertheless, the local maximum of NGMS in this area does not persist, and the NGMS drops to small values on 11 October before increasing gradually again, as in other longitudes. The two MJO events also differ quantitatively: the November event has larger maximum NGMS and propagates faster than the October event.

In summary, the basic features of the observationally derived temporal and spatial evolution of the NGMS in the WRF simulation are consistent with those in observations as shown in S14. This temporal variation of the NGMS as an integral part of the MJO life cycle has yet to be incorporated in any theoretical models, to our knowledge.

5. Summary and conclusions

Several MJO events in the equatorial Indian Ocean were observed during the international CINDY/DYNAMO

field campaign from October 2011 to March 2012. This study focuses on the October and November MJO events as simulated by a regional model at horizontal grid spacing of 9 km. Results from the simulation are compared quantitatively to multiple observational datasets. The main results are summarized as follows:

1) The simulation captures both the October and November MJO events. Slow eastward progression of the MJO active phase at a speed of 5–7 m s^{-1} is well simulated. Large-scale vertical motion in the simulation has weak ascent in the leading edge of the MJO envelope, followed by deep ascent with first baroclinic mode structure during the peak precipitation stage and trailed by second baroclinic mode structure with ascent in the upper troposphere and descent in the lower troposphere. The trailing ascent/descent region is associated with significant net column radiation anomalies and broadens significantly because of its westward expansion during the eastward propagation of the MJO events.

2) Along with the eastward propagation, both the simulated and observed MJO events also have a slow northward propagation component (~1 m s^{-1}). Two tropical cyclone events closely related to the MJO events are observed. The WRF simulates similar TC structures to those in observations but with weaker amplitudes. Significant high-frequency westward-propagating convective activity is found within the MJO envelope in the 3-hourly rainfall field. A wave-number–frequency diagram of satellite-retrieved rainfall indicates that these are westward inertia–gravity waves with phase speeds of 10–22 m s^{-1}. The model captures similar wave signals in the frequency–wavenumber domain.

3) Comparison with the observations from the northern sounding array (Johnson and Ciesielski 2013) indicates that the model simulates the passage of the two MJO events over the northern sounding array region well: rainfall peaks over 30 mm day^{-1} during late October and November, OLR drops by more than 100 W m^{-2}, and reflected shortwave radiation increases by more than 150 W m^{-2}. Simulated large-scale vertical velocity over the NSA follows the shallow convection, deep ascent, and ascent/descent sequence that are also found in the vertical motion deduced from observations. The time-mean vertical velocity is 1.1×10^{-2} m s^{-1}, close in amplitude to the NSA-derived value (~1.2×10^{-2} m s^{-1}). Lower-tropospheric westerlies gradually deepen during the October MJO event while the upper-tropospheric easterlies strengthen. Temperature anomalies develop first at low levels and later in the upper

troposphere, where they attain maxima on the order of 1–2 K. This time sequence indicates a westward tilt structure in the longitude–height plane, which appears to be a general MJO feature as found in previous studies (e.g., Benedict and Randall 2007; Kim et al. 2009; Wu and Deng 2013).

4) In numerical experiments with daily SST replaced by time-independent SST, the October MJO event is well reproduced in both 850-hPa zonal winds and surface precipitation, but the simulation of the November event is much degraded. This suggests that daily SST plays an important role for the November MJO event but much less so for the October event.

5) Analysis of the moist static energy budget shows that both advection and diabatic processes contribute to the MSE buildup, but their contributions differ in the lead time prior to the precipitation peak in a manner broadly consistent with earlier studies. The MSE budget is reasonably balanced without explicitly accounting for subgrid-scale transports if all variables are averaged at the effective model resolution (~7 times the grid spacing).

6) While the free-running WRF simulation captures many aspects of the MJO events qualitatively, quantitative model biases are also apparent, notably in the following: (i) the simulated November MJO event is delayed by 3 days and also weaker than observations; (ii) the model shows high values of surface flux during the first MJO event, while there is no increase in the flux in the observations; (iii) while the MJO precipitation anomalies are greater in the model than in observations, anomalies in OLR and column net radiation are weaker, suggesting that model has a weaker radiative feedback than the real atmosphere; (iv) the ITCZ in the Southern Hemisphere (south of 5°S) is not well simulated in the model; and (v) vertical advection of moist static energy is positive in the time mean (~50 W m^{-2}), in contrast to negative values (~-22 W m^{-2}) derived from the sounding array observation. Horizontal advection of MSE is ~-100 W m^{-2}, which is also less than observational value (~-26 W m^{-2}). The relative stronger surface flux feedback and weaker cloud–radiative feedback compensate each other to some extent. Similarly, horizontal advection and vertical advection of MSE also show a good degree of compensation.

REFERENCES

Anber, U., S. Wang, and A. H. Sobel, 2014: Response of atmospheric convection to vertical wind shear: Cloud-system resolving simulations with parameterized large-scale circulation. Part I: Specified radiative cooling. *J. Atmos. Sci.,* **71,** 2976–2993, doi:10.1175/JAS-D-13-0320.1.

Andersen, J. A., and Z. Kuang, 2012: Moist static energy budget of MJO-like disturbances in the atmosphere of a zonally symmetric aquaplanet. *J. Climate,* **25,** 2782–2804, doi:10.1175/JCLI-D-11-00168.1.

Benedict, J. J., and D. A. Randall, 2007: Observed characteristics of the MJO relative to maximum rainfall. *J. Atmos. Sci.,* **64,** 2332–2354, doi:10.1175/JAS3968.1.

——, E. Maloney, A. H. Sobel, and D. M. Frierson, 2014: Gross moist stability and MJO simulation skill in three full-physics GCMs. *J. Atmos. Sci.,* **71,** 3327–3349, doi:10.1175/JAS-D-13-0240.1.

Bony, S., and K. A. Emanuel, 2005: On the role of moist processes in tropical intraseasonal variability: Cloud–radiation and moisture–convection feedbacks. *J. Atmos. Sci.,* **62,** 2770–2789, doi:10.1175/JAS3506.1.

Chen, F., and J. Dudhia, 2001: Coupling an advanced land surface-hydrology model with the Penn State–NCAR MM5 modeling system. Part I: Model implementation and sensitivity. *Mon. Wea. Rev.,* **129,** 569–585, doi:10.1175/1520-0493(2001)129<0569:CAALSH>2.0.CO;2.

Chou, M. D., and M. J. Suarez, 1994: An efficient thermal infrared radiation parameterization for use in general circulation models. NASA Tech. Memo. 104606, 98 pp.

Ciesielski, P. E., and Coauthors, 2014: Quality-controlled upper-air sounding dataset for DYNAMO/CINDY/AMIE: Development and corrections. *J. Atmos. Oceanic Technol.,* **31,** 741–764, doi:10.1175/JTECH-D-13-00165.1.

Dee, D. P., and Coauthors, 2011: The ERA-Interim reanalysis: Configuration and performance of the data assimilation system. *Quart. J. Roy. Meteor. Soc.,* **137,** 553–597, doi:10.1002/qj.828.

Del Genio, A. D., Y. Chen, D. Kim, and M.-S. Yao, 2012: The MJO transition from shallow to deep convection in *CloudSat/* CALIPSO data and GISS GCM simulations. *J. Climate,* **25,** 3755–3770, doi:10.1175/JCLI-D-11-00384.1.

Emanuel, K. A., 1987: An air-sea interaction model of intraseasonal oscillations in the tropics. *J. Atmos. Sci.,* **44,** 2324–2340, doi:10.1175/1520-0469(1987)044<2324:AASIMO>2.0.CO;2.

Fu, X., J.-Y. Lee, P.-C. Hsu, H. Taniguchi, B. Wang, W. Wang, and S. Weaver, 2013: Multi-model MJO forecasting during DYNAMO/CINDY period. *Climate Dyn.,* **41,** 1067–1081, doi:10.1007/s00382-013-1859-9.

——, W. Wang, J.-Y. Lee, B. Wang, K. Kikuchi, J. Xu, and S. Weaver, 2015: Distinctive roles of air–sea coupling on different MJO events: A new perspective revealed from the DYNAMO/CINDY field campaign. *Mon. Wea. Rev.,* doi:10.1175/MWR-D-14-00221.1, in press.

Fuchs, Ž., and D. J. Raymond, 2002: Large-scale modes of a non-rotating atmosphere with water vapor and cloud–radiation feedbacks. *J. Atmos. Sci.,* **59,** 1669–1679, doi:10.1175/1520-0469(2002)059<1669:LSMOAN>2.0.CO;2.

Gill, A. E., 1980: Some simple solutions for heat-induced tropical circulation. *Quart. J. Roy. Meteor. Soc.,* **106,** 447–462, doi:10.1002/qj.49710644905.

Gottschalck, J., P. E. Roundy, C. J. Schreck III, A. Vintzileos, and C. Zhang, 2013: Large-scale atmospheric and oceanic conditions during the 2011–12 DYNAMO field campaign. *Mon. Wea. Rev.,* **141,** 4173–4196, doi:10.1175/MWR-D-13-00022.1.

Hagos, S., and L. R. Leung, 2011: Moist thermodynamics of the Madden–Julian oscillation in a cloud-resolving simulation. *J. Climate,* **24,** 5571–5583, doi:10.1175/2011JCLI4212.1.

——, ——, and J. Duddhia, 2011: Thermodynamics of the Madden–Julian oscillation in a regional model with constrained moisture. *J. Atmos. Sci.,* **68,** 1974–1989, doi:10.1175/2011JAS3592.1.

Holloway, C. E., S. J. Woolnough, and G. M. S. Lister, 2013: The effects of explicit versus parameterized convection on the MJO in a Large-domain high-resolution tropical case study. Part I: Characterization of large-scale organization and propagation. *J. Atmos. Sci.,* **70,** 1342–1369, doi:10.1175/JAS-D-12-0227.1.

Hong, S.-Y., Y. Noh, and J. Dudhia, 2006: A new vertical diffusion package with an explicit treatment of entrainment processes. *Mon. Wea. Rev.,* **134,** 2318–2341, doi:10.1175/MWR3199.1.

Houze, R. A., Jr., S. S. Chen, D. E. Kingsmill, Y. Serra, and S. E. Yuter, 2000: Convection over the Pacific warm pool in relation to the atmospheric Kelvin–Rossby wave. *J. Atmos. Sci.,* **57,** 3058–3089, doi:10.1175/1520-0469(2000)057<3058:COTPWP>2.0.CO;2.

Hsu, P.-C., and T. Li, 2012: Role of the boundary layer moisture asymmetry in causing the eastward propagation of the Madden–Julian oscillation. *J. Climate,* **25,** 4914–4931, doi:10.1175/JCLI-D-11-00310.1.

Hu, Q., and D. A. Randall, 1994: Low-frequency oscillations in radiative-convective systems. *J. Atmos. Sci.,* **51,** 1089–1099, doi:10.1175/1520-0469(1994)051<1089:LFOIRC>2.0.CO;2.

Hung, M.-P., J.-L. Lin, W. Wang, D. Kim, T. Shinoda, and S. J. Weaver, 2013: MJO and convectively coupled equatorial waves simulated by CMIP5 climate models. *J. Climate,* **26,** 6185–6214, doi:10.1175/JCLI-D-12-00541.1.

Iacono, M. J., J. S. Delamere, E. J. Mlawer, M. W. Shephard, S. A. Clough, and W. D. Collins, 2008: Radiative forcing by long-lived greenhouse gases: Calculations with the AER radiative transfer models. *J. Geophys. Res.,* **113,** D13103, doi:10.1029/2008JD009944.

Johnson, R. H., and P. E. Ciesielski, 2013: Structure and properties of Madden–Julian oscillations deduced from DYNAMO sounding arrays. *J. Atmos. Sci.,* **70,** 3157–3179, doi:10.1175/JAS-D-13-065.1.

Joyce, R. J., J. E. Janowiak, P. A. Arkin, and P. Xie, 2004: CMORPH: A method that produces global precipitation estimates from passive microwave and infrared data at high spatial and temporal resolution. *J. Hydrometeor.,* **5,** 487–503, doi:10.1175/1525-7541(2004)005<0487:CAMTPG>2.0.CO;2.

Jung, T., and Coauthors, 2012: High-resolution global climate simulations with the ECMWF model in Project Athena: Experimental design, model climate, and seasonal forecast skill. *J. Climate,* **25,** 3155–3172, doi:10.1175/JCLI-D-11-00265.1.

Kerns, B. W., and S. S. Chen, 2013: Equatorial dry air intrusion and related synoptic variability in MJO initiation during DYNAMO. *Mon. Wea. Rev.,* **142,** 1326–1343, doi:10.1175/MWR-D-13-00159.1.

Khouider, B., and Y. Han, 2013: Simulation of convectively coupled waves using WRF: A framework for assessing the effects of mesoscales on synoptic scales.*Theor. Comput. Fluid Dyn.,* **27,** 473–489, doi:10.1007/s00162-012-0276-8.

Kiladis, G. N., K. H. Straub, and P. T. Haertel, 2005: Zonal and vertical structure of the Madden–Julian oscillation. *J. Atmos. Sci.,* **62,** 2790–2809, doi:10.1175/JAS3520.1.

——, M. C. Wheeler, P. T. Haertel, K. H. Straub, and P. E. Roundy, 2009: Convectively coupled equatorial waves. *Rev. Geophys.,* **47,** RG2003, doi:10.1029/2008RG000266.

Kim, D., and Coauthors, 2009: Application of MJO simulation diagnostics to climate models. *J. Climate,* **22,** 6413–6436, doi:10.1175/2009JCLI3063.1.

——, A. H. Sobel, E. D. Maloney, D. M. W. Frierson, and I.-S. Kang, 2011: A systematic relationship between intraseasonal variability and mean state bias in AGCM simulations. *J. Climate,* **24,** 5506–5520, doi:10.1175/2011JCLI4177.1.

——, J.-S. Kug, and A. H. Sobel, 2014: Propagating versus nonpropagating Madden–Julian oscillation events. *J. Climate,* **27,** 111–125, doi:10.1175/JCLI-D-13-00084.1.

Kiranmayi, L., and E. D. Maloney, 2011: Intraseasonal moist static energy budget in reanalysis data. *J. Geophys. Res.,* **116,** D21117, doi:10.1029/2011JD016031.

Klemp, J. B., J. Dudhia, and A. D. Hassiotis, 2008: An upper gravity-wave absorbing layer for NWP applications. *Mon. Wea. Rev.,* **136,** 3987–4004, doi:10.1175/2008MWR2596.1.

Lee, M.-I., I.-S. Kang, J.-K. Kim, and B. E. Mapes, 2001: Influence of cloud-radiation interaction on simulating tropical intraseasonal oscillation with an atmospheric general circulation model. *J. Geophys. Res.,* **106,** 14 219–14 233, doi:10.1029/2001JD900143.

Lim, K.-S. S., and S.-Y. Hong, 2010: Development of an effective double-moment cloud microphysics scheme with prognostic cloud condensation nuclei (CCN) for weather and climate models. *Mon. Wea. Rev.,* **138,** 1587–1612, doi:10.1175/2009MWR2968.1.

Lin, J.-L., and Coauthors, 2006: Tropical intraseasonal variability in 14 IPCC AR4 climate models. Part I: Convective signals. *J. Climate,* **19,** 2665–2690, doi:10.1175/JCLI3735.1.

Lin, X., and R. H. Johnson, 1996: Kinematic and thermodynamic characteristics of the flow over the western Pacific warm pool during TOGA/COARE. *J. Atmos. Sci.,* **53,** 695–715, doi:10.1175/1520-0469(1996)053<0695:KATCOT>2.0.CO;2.

Ling, J., P. Bauer, P. Bechtold, A. Beljaars, R. Forbes, F. Vitart, M. Ulate, and C. Zhang, 2014: Global versus local MJO forecast skill of the ECMWF model during DYNAMO. *Mon. Wea. Rev.,* **142,** 2228–2247, doi:10.1175/MWR-D-13-00292.1.

Loeb, N. G., S. Kato, W. Su, T. Wong, F. G. Rose, D. R. Doelling, J. R. Norris, and X. Huang, 2012: Advances in understanding top-of-atmosphere radiation variability from satellite observations. *Surv. Geophys.,* **33,** 359–385, doi:10.1007/s10712-012-9175-1.

Madden, R. A., and P. R. Julian, 1971: Detection of a 40–50 day oscillation in the zonal wind in the tropical Pacific. *J. Atmos. Sci.,* **28,** 702–708, doi:10.1175/1520-0469(1971)028<0702:DOADOI>2.0.CO;2.

——, and ——, 1972: Description of global-scale circulation cells in tropics with a 40–50 day period. *J. Atmos. Sci.,* **29,** 1109–1123, doi:10.1175/1520-0469(1972)029<1109:DOGSCC>2.0.CO;2.

Majda, A. J., and S. N. Stechmann, 2009: A simple dynamical model with features of convective momentum transport. *J. Atmos. Sci.,* **66,** 373–392, doi:10.1175/2008JAS2805.1.

Maloney, E. D., 2009: The moist static energy budget of a composite tropical intraseasonal oscillation in a climate model. *J. Climate,* **22,** 711–729, doi:10.1175/2008JCLI2542.1.

——, A. H. Sobel, and W. M. Hannah, 2010: Intraseasonal variability in an aquaplanet general circulation model. *J. Adv. Model. Earth. Syst.,* **2,** 5, doi:10.3894/JAMES.2010.2.5.

Mapes, B. E., and J. T. Bacmeister, 2012: Diagnosing tropical biases and the MJO using patterns in MERRA's analysis tendencies. *J. Climate,* **25,** 6202–6214, doi:10.1175/JCLI-D-11-00424.1.

——, S. Tulich, J.-L. Lin, and P. Zuidema, 2006: The mesoscale convection life cycle: Building block or prototype for large-scale tropical waves? *Dyn. Atmos. Oceans,* **42,** 3–29, doi:10.1016/j.dynatmoce.2006.03.003.

Miura, H., M. Satoh, T. Nasuno, A. T. Noda, and K. Oouchi, 2007: A Madden–Julian Oscillation event realistically simulated by a global cloud-resolving model. *Science,* **318,** 1763–1765, doi:10.1126/science.1148443.

Miyakawa, T., and Coauthors, 2014: Madden–Julian oscillation prediction skill of a new-generation global model. *Nat. Commun.,* **5,** 3769, doi:10.1038/ncomms4769.

Moum, J. N., and Coauthors, 2013: Air–sea interactions from westerly wind bursts during the November 2011 MJO in the Indian Ocean. *Bull. Amer. Meteor. Soc.,* **95,** 1185–1199, doi:10.1175/BAMS-D-12-00225.1.

Neelin, J. D., 2007: Moist dynamics of tropical convection zones in monsoons, teleconnections and global warming. *The Global Circulation of the Atmosphere,* T. Schneider and A. Sobel, Eds., Princeton University Press, 267–301.

——, and I. M. Held, 1987: Modeling tropical convergence based on the moist static energy budget. *Mon. Wea. Rev.,* **115,** 3–12, doi:10.1175/1520-0493(1987)115<0003:MTCBOT>2.0.CO;2.

——, ——, and K. H. Cook, 1987: Evaporation-wind feedback and low frequency variability in the tropical atmosphere. *J. Atmos. Sci.,* **44,** 2341–2348, doi:10.1175/1520-0469(1987)044<2341:EWFALF>2.0.CO;2.

Powell, S. W., and R. A. Houze, 2013: The cloud population and onset of the Madden-Julian oscillation over the Indian Ocean during DYNAMO-AMIE. *J. Geophys. Res.,* **118,** 11 979–11 995, doi:10.1002/2013JD020421.

Ray, P., and C. Zhang, 2010: A case study of the mechanics of extratropical influence on the initiation of the Madden–Julian oscillation. *J. Atmos. Sci.,* **67,** 515–528, doi:10.1175/2009JAS3059.1.

——, ——, J. Dudhia, and S. S. Chen, 2009: A numerical case study on the initiation of the Madden–Julian oscillation. *J. Atmos. Sci.,* **66,** 310–331, doi:10.1175/2008JAS2701.1.

Raymond, D. J., 2001: A new model of the Madden–Julian oscillation. *J. Atmos. Sci.,* **58,** 2807–2819, doi:10.1175/1520-0469(2001)058<2807:ANMOTM>2.0.CO;2.

——, and Ž. Fuchs, 2007: Convectively coupled gravity and moisture modes in a simple atmospheric model. *Tellus,* **59A,** 627–640, doi:10.1111/j.1600-0870.2007.00268.x.

——, and ——, 2009: Moisture modes and the Madden–Julian oscillation. *J. Climate,* **22,** 3031–3046, doi:10.1175/2008JCLI2739.1.

——, S. Sessions, A. H. Sobel, and Ž. Fuchs, 2009: The mechanics of gross moist stability. *J. Adv. Model. Earth Syst.,* **1,** 9, doi:10.3894/JAMES.2009.1.9.

Seo, H., A. C. Subramanian, A. J. Miller, and N. R. Cavanaugh, 2014: Coupled impacts of the diurnal cycle of sea surface temperature on the Madden–Julian oscillation. *J. Climate,* **27,** 8422–8443, doi:10.1175/JCLI-D-14-00141.1.

Shi, J. J., and Coauthors, 2010: WRF simulations of the 20–22 January 2007 snow events over eastern Canada: Comparison with in situ and satellite observations. *J. Appl. Meteor. Climatol.,* **49,** 2246–2266, doi:10.1175/2010JAMC2282.1.

Skamarock, W. C., 2004: Evaluating mesoscale NWP models using kinetic energy spectra. *Mon. Wea. Rev.,* **132,** 3019–3032, doi:10.1175/MWR2830.1.

——, and Coauthors, 2008: A description of the Advanced Research WRF version 3. NCAR Tech. Note NCAR/TN-475+STR, 125 pp.

Sobel, A. H., 2007, Simple models of ensemble averaged precipitation and surface wind, given the SST. *The Global Circulation of the Atmosphere,* T. Schneider and A. H. Sobel, Eds., Princeton University Press, 219–251.

——, and E. Maloney, 2012: An idealized semi-empirical framework for modeling the Madden–Julian oscillation. *J. Atmos. Sci.,* **69,** 1691–1705, doi:10.1175/JAS-D-11-0118.1.

——, and ——, 2013: Moisture modes and the eastward propagation of the MJO. *J. Atmos. Sci.,* **70,** 187–192, doi:10.1175/JAS-D-12-0189.1.

——, J. Nilsson, and L. M. Polvani, 2001: The weak temperature gradient approximation and balanced tropical moisture waves. *J. Atmos. Sci.,* **58,** 3650–3665, doi:10.1175/1520-0469(2001)058<3650:TWTGAA>2.0.CO;2.

——, E. Maloney, G. Bellon, and D. F. M. Frierson, 2008: The role of surface fluxes in tropical intraseasonal oscillations. *Nat. Geosci.,* **1,** 653–657, doi:10.1038/ngeo312.

——, ——, ——, and ——, 2010: Surface fluxes and tropical intraseasonal variability: A reassessment. *J. Adv. Model. Earth Syst.,* **2,** 2, doi:10.3894/JAMES.2010.2.2.

——, S. Wang, and D. Kim, 2014: Moist static energy budget of the MJO during DYNAMO. *J. Atmos. Sci.,* **71,** 4276–4291, doi:10.1175/JAS-D-14-0052.1.

Takayabu, Y. N., K.-M. Lau, and C.-H. Sui, 1996: Observation of a quasi-2-day wave during TOGA COARE. *Mon. Wea. Rev.,* **124,** 1892–1913, doi:10.1175/1520-0493(1996)124<1892:OOAQDW>2.0.CO;2.

Thayer-Calder, K., and D. A. Randall, 2009: The role of convective moistening in the Madden–Julian oscillation. *J. Atmos. Sci.,* **66,** 3297–3312, doi:10.1175/2009JAS3081.1.

Tulich, S. N., and G. N. Kiladis, 2012: Squall lines and convectively coupled gravity waves in the tropics: Why do most cloud systems propagate westward? *J. Atmos. Sci.,* **69,** 2995–3012, doi:10.1175/JAS-D-11-0297.1.

Virts, K. S., and J. M. Wallace, 2010: Annual, interannual, and intraseasonal variability of tropical tropopause transition layer cirrus. *J. Atmos. Sci.,* **67,** 3097–3112, doi:10.1175/2010JAS3413.1.

Vitart, F., 2009: Impact of the Madden–Julian oscillation on tropical storms and risk of landfall in the ECMWF forecast system. *Geophys. Res. Lett.,* **36,** L15802, doi:10.1029/2009GL039089.

——, A. Leroy, and M. C. Wheeler, 2010: A comparison of dynamical and statistical predictions of weekly tropical cyclone activity in the Southern Hemisphere. *Mon. Wea. Rev.,* **138,** 3671–3682, doi:10.1175/2010MWR3343.1.

Wang, B., 1988: Dynamics of tropical low-frequency waves: An analysis of the moist Kelvin wave. *J. Atmos. Sci.,* **45,** 2051–2065, doi:10.1175/1520-0469(1988)045<2051:DOTLFW>2.0.CO;2.

——, and H. Rui, 1990: Dynamics of the coupled moist Kelvin–Rossby wave on an equatorial β-plane. *J. Atmos. Sci.,* **47,** 397–413, doi:10.1175/1520-0469(1990)047<0397:DOTCMK>2.0.CO;2.

Wang, S., and A. H. Sobel, 2011: Response of convection to relative sea surface temperature: Cloud resolving simulations in two and three dimensions. *J. Geophys. Res.,* **116,** D11119, doi:10.1029/2010JD015347.

——, and ——, 2012: Impact of imposed drying on deep convection in a cloud-resolving model. *J. Geophys. Res.,* **117,** D02112, doi:10.1029/2011JD016847.

——, ——, and Z. Kuang, 2013: Cloud-resolving simulation of TOGA-COARE using parameterized large-scale dynamics. *J. Geophys. Res. Atmos.,* **118,** 6290–6301, doi:10.1002/jgrd.50510.

Wheeler, M., and G. N. Kiladis, 1999: Convectively coupled equatorial waves: Analysis of clouds and temperature in the wavenumber–frequency domain. *J. Atmos. Sci.,* **56,** 374–399, doi:10.1175/1520-0469(1999)056<0374:CCEWAO>2.0.CO;2.

Wielicki, B. A., B. R. Barkstrom, E. F. Harrison, E. B. Lee III, G. L. Smith, and J. E. Cooper, 1996: Clouds and the Earth's Radiant Energy System (CERES): An Earth Observing System experiment. *Bull. Amer. Meteor. Soc.,* **77,** 853–868, doi:10.1175/1520-0477(1996)077<0853:CATERE>2.0.CO;2.

Wu, X., and L. Deng, 2013: Comparison of moist static energy and budget between the GCM-simulated Madden–Julian oscillation and observations over the Indian Ocean and western Pacific. *J. Climate,* **26,** 4981–4993, doi:10.1175/JCLI-D-12-00607.1.

Wu, Z., 2003: A shallow CISK, deep equilibrium mechanism for the interaction between large-scale convection and large-scale circulations in the tropics. *J. Atmos. Sci.,* **60,** 377–392, doi:10.1175/1520-0469(2003)060<0377:ASCDEM>2.0.CO;2.

Yu, X., and T.-Y. Lee, 2010: Role of convective parameterization in simulations of a convection band at grey-zone resolutions. *Tellus,* **62,** 617–632, doi:10.1111/j.1600-0870.2010.00470.x.

Yoneyama, K., C. Zhang, and C. N. Long, 2013: Tracking pulses of the Madden–Julian oscillation. *Bull. Amer. Meteor. Soc.,* **94,** 1871–1891, doi:10.1175/BAMS-D-12-00157.1.

Zeng, X., and A. Beljaars, 2005: A prognostic scheme of sea surface skin temperature for modeling and data assimilation. *Geophys. Res. Lett.,* **32,** L14605, doi:10.1029/2005GL023030.

Zhang, C., 2005: Madden-Julian oscillation. *Rev. Geophys.,* **43,** RG2003, doi:10.1029/2004RG000158.

——, J. Gottschalck, E. D. Maloney, M. W. Moncrieff, F. Vitart, D. E. Waliser, B. Wang, and M. C. Wheeler, 2013: Cracking the MJO nut. *Geophys. Res. Lett.,* **40,** 1223–1230, doi:10.1002/grl.50244.

Zhang, G. J., and X. Song, 2009: Interaction of deep and shallow convection is key to Madden-Julian Oscillation simulation. *Geophys. Res. Lett.,* **36,** L09708, doi:10.1029/2009GL037340.

Zhou, L., and I.-S. Kang, 2013: Influence of convective momentum transport on mixed Rossby–gravity waves: A contribution to tropical 2-day waves. *J. Atmos. Sci.,* **70,** 2467–2475, doi:10.1175/JAS-D-12-0300.1.

Zuluaga, M. D., and R. A. Houze Jr., 2013: Evolution of the population of precipitating convective systems over the equatorial Indian Ocean in active phases of the Madden–Julian oscillation. *J. Atmos. Sci.,* **70,** 2713–2725, doi:10.1175/JAS-D-12-0311.1.